

Title: Design and Evaluation of Photodynamically Active Lipid-Based Nanoformulations for Combination Therapy against Skin Cancer

Abstract

Skin cancer (SC) is the fourth most common type of cancer in the whole world. The main two subtypes that cover 95% of all cases are melanoma and non-melanoma skin cancer (NMSC). Non-melanoma skin cancer is a type of cutaneous malignancy and the most observed cancer in people. In NMSC involved Basal cell carcinoma (BCC), squamous cell carcinoma (SCC), extramammary Paget's disease (EMPD), Merkel cell carcinoma (MCC), and several carcinomas. In the NMSC, 70 to 80 % of skin cancer arises from BSC, and 20 to 25 % is responsible by SCC. According to the Italian Association for Cancer Research (AIRC), cutaneous melanoma makes up only 5% of skin tumors. Due to its rapid metastasis, melanoma remains one of the deadliest types of skin cancer. Several treatment options are available for skin cancer (malignant melanoma (MM) and NMSC), depending on the type, stage, and location of the cancer. Primary treatment modalities include surgery, radiation, topical, targeted, immunotherapy, and chemotherapy. Oral chemotherapy is non-invasive and does not require surgical procedures or radiation therapy. However, there are also limitations to oral chemotherapy for skin cancer. The effectiveness of oral chemotherapy can vary depending on the type and stage of skin cancer, and it may not be the most effective option for all cases. Furthermore, oral chemotherapy can have side effects, including nausea, vomiting, fatigue, and decreased blood cell counts, and lack of precision in oral chemotherapy can lead to the destruction of healthy cells.

Topical chemotherapy for skin cancer is commonly utilized as a cost-effective and convenient treatment approach and is non-invasive and localized in nature, as the medication is directly applied to the affected area. This targeted approach minimizes systemic side effects while effectively treating superficial skin cancers. The convenience and ease of use of topical chemotherapy allow patients to self-administer the treatment at home. Furthermore, it preserves healthy tissue and offers better cosmetic outcomes than surgical interventions or radiation therapy. However, topical monotherapy for skin cancer has certain drawbacks, including the potential risk of metastasis. While topical treatments are effective for superficial skin cancers, they may not adequately address deeper or more aggressive forms of skin cancer. These cancers have the potential to invade deeper layers of the skin and spread to other parts of the body, leading to metastasis. Topical medications primarily target the surface layers of the skin, and their limited penetration may not be sufficient to eliminate cancer cells that have already spread beyond the initial site. Therefore, relying solely on topical monotherapy for advanced or metastatic skin cancer may not be sufficient in controlling or eradicating skin cancer. In such cases, a combination of treatments, including Photodynamic Therapy (PDT) and topical chemotherapy, may be necessary to address the risk of metastasis and achieve better treatment outcomes.

PDT offers the benefit of being a non-invasive treatment option that can be applied over a wide treatment area, yielding favorable clinical outcomes. Several clinical research studies have demonstrated the effectiveness of PDT in the treatment of pre-malignant and malignant non-melanoma skin cancer (NMSC). However, it presents certain drawbacks, including limited tumor penetration, insufficient light penetration, prolonged chemotherapy leading to drug resistance, metastasis appear, and sometimes becoming more aggressive and ultimately resulting in ineffective therapy. In this sense, enhancing PDT effectiveness by combining it with other therapeutic modalities has become an interesting field in melanoma and NMSC research.

In this aspect, topical administration of anticancer drugs along with photodynamically active molecules is a non-invasive approach, which stands to be a promising modality for treating aggressive cutaneous melanomas and basal cell carcinoma with the added advantage of synergistic effect and high patient compliance. Most of the drug molecules that have been discovered and are being used in pharmaceuticals are hydrophobic in nature, thereby posing challenges in their delivery. Its conventional preparations (gels, creams, ointments, etc.) exhibit lower efficacy and cause local toxicity due to rapid loco-regional drug release. To avoid these toxicities and problems associated with above mentioned and improve the efficacy of compounds, new carriers are required that should penetrate deeper into the viable epidermis or tumor tissues. In order to address these challenges, the focus has been switched to nanotherapeutics. Several reports state that lipidic nano-carriers are preferred for their promising delivery of therapeutic agents to localized skin surfaces due to their smaller size, greater permeation through biological barriers, better surface properties, high skin deposition, and sustained drug release properties; they were able to prove advantageous in treating skin cancer, including basal cell carcinoma and melanoma.

In this dissertation, the combination of dual-drug lipidic nanoparticles was explored for the topical delivery of Itraconazole (ITZ) as an anticancer agent and Chlorin e6 (Ce6) as a photoactivable molecule for treating skin cancer (Basal Cell Carcinoma and Melanoma cancer) using photodynamic therapy.

A simple and accurate HPLC analytical method was developed and validated to estimate the ITZ in the drug release, ex-vivo skin permeation study. A fluorescence spectrofluorometric method was developed to estimate chlorin e6 levels in samples obtained from drug release studies, ex-vivo experiments, etc. The initial optimization of the formulation was conducted using the QbD approach with the ITZ, and the final optimized batch was formulated with chlorin e6 instead. The process of preparing a combined batch of dual drug lipidic nanoparticles (ITZ/Ce6@LNPs) involved hot emulsification, followed by size reduction using probe sonication. The optimized dual drug lipidic nanoparticle containing itraconazole and chlorin e6 exhibited a particle size of less than 100 nm, and entrapment efficiency for both molecules were found to be less than 81%. Our results depicted that topically applying this reactive oxygen species (ROS) generative dual drug-loaded lipidic nanoparticles incorporated in SEPINEO gel

achieves better permeation ($78 \pm 7.34 \%$) across the skin and exhibited the higher skin retention. The therapeutic efficacy of the developed formulation was tested on B16F10 and A431 cell lines via cellular uptake, cytotoxicity evaluation, combination index Mitochondrial membrane potential, nuclear staining, DNA fragmentation, ROS generation, apoptosis, and cell cycle assays under NIR irradiation (665 nm at 0.5 W/cm^2). Co-delivering ITZ and Ce6 exhibited synergistic effects, higher cellular uptake, better cancer growth inhibition, and pronounced apoptotic events compared to the free drug-alone formulation. ITZ/Ce6@LNPs treatment showed the lowest IC_{50} values compared to free Ce6 and free ITZ. The ~ 3.1 fold decrease in IC_{50} values of ITZ/Ce6@LNPs than free Ce6 and free ITZ at 24 h in the presence of laser treatment. Therefore, it indicated that the longer retention of ITZ/Ce6@LNPs intracellularly reaches optimum concentration to exert cytotoxic action. Interestingly, a combination of ITZ and Ce6 lipidic nanoformulation showed higher apoptosis on the B16F10 and A431 cell lines than free drugs. Flow cytometry analysis demonstrated that ITZ/Ce6@LNPs exhibited more mitochondria membrane potential disruption in B16F10 and A431 cell lines. In the ex-vivo permeation study, it was observed that ITZ/Ce6@LNPs gel exhibited a permeation rate of up to 78% through the skin after 24 h, whereas the plain gel (ITZ+Ce6) showed a permeation rate of 30%. Further In-vivo topical biodistribution study was tested on the B16F10 cell-induced tumor-bearing mice model. The findings revealed that the fluorescence intensity of the ITZ/Ce6@LNPs gel increased at the tumor site for up to 12 h following topical application. In contrast, the group treated with free Ce6 exhibited a significantly lower signal, indicated that the ITZ/Ce6@LNPs gel has the potential to accumulate gradually at the tumor site. Further tumors were separated, and their major organs were collected for fluorescence imaging. However, some measurable ITZ/Ce6@LNPs fluorescence was present in the tumor, resulting in a significantly higher accumulation of ITZ/Ce6@LNPs observed in the tumor tissue. It suggests that ITZ/Ce6@LNPs selectively accumulated in the target tissue (superficial skin cancer), which is a desirable outcome for the designed formulation.

After observing the impressive combined chemo-photodynamic therapeutic effects of the ITZ/Ce6/LNPs gel in vitro studies, we proceeded to investigate its vivo anticancer potential. The developed ITZ/Ce6@LNPs gel exhibited the slowest tumor growth compared to the treatment group. The enhanced delivery of potent molecules to the tumor site led to a remarkable improvement in the in vivo anti-tumor efficacy against a C57 skin cancer mouse model. This improvement was characterized by increased generation of reactive oxygen species (ROS) and induction of apoptosis within the tumor. The average tumor volumes post eight days were $708 \pm 31 \text{ mm}^3$, $502 \pm 10 \text{ mm}^3$, $545 \pm 17 \text{ mm}^3$, $402 \pm 10 \text{ mm}^3$, $170 \pm 18 \text{ mm}^3$ for control, free Ce6, ITZ, ITZ+Ce6 and ITZ/Ce6/LNPs gel, respectively

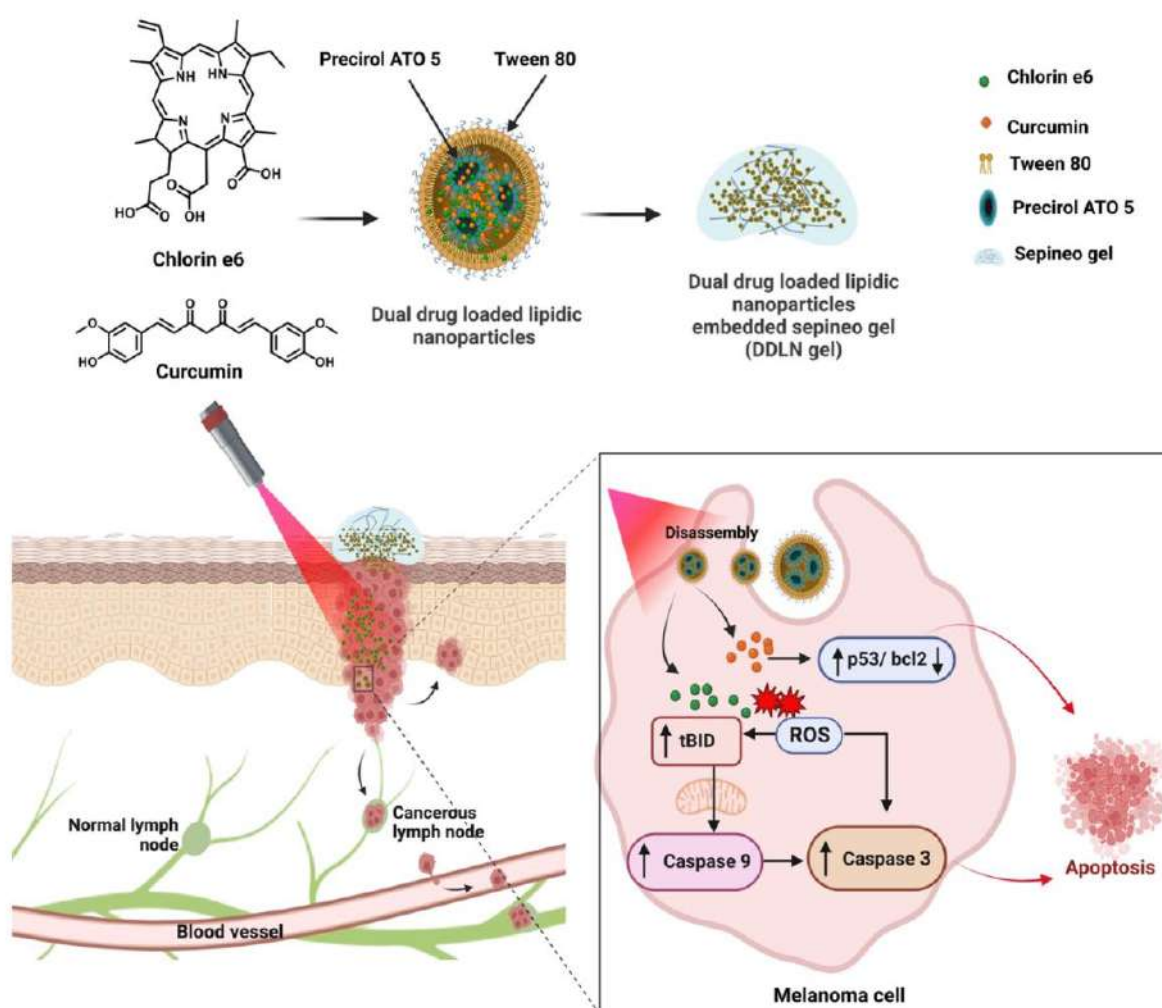
The ROS and TUNEL assay demonstrated a greater intensity of bright green fluorescence in tumor samples treated with the in-house developed gel, indicating an increased presence of apoptotic bodies and significant production of reactive oxygen species (ROS). Conversely, in the Ki-67 assay, the control group exhibited higher cell proliferation, as indicated by the strongest green fluorescence, while the in-

house developed gel treatment group displayed lower green fluorescence, suggesting reduced cell proliferation.. This indicates that the in-house developed gel treatment resulted in reduced Ki-67 positive tumor cells and confirmed minimal tumor growth.

In another study, we have formulated dual drug lipidic nanoparticles using as a natural anticancer agent, including curcumin (CUR) and Chlorin e6 (Ce6) for the treatment of skin cancer (Melanoma and Basal cell carcinoma). Curcumin, an active anticancer agent, and chlorin e6, a photoactivable molecule, were developed into dual drug-based lipidic nanoparticles that produced (ROS) when activated at 665 nm by Near-infrared light (NIR). A simple and accurate simultaneous HPLC analytical method was developed and validated to estimate the CUR and Ce6 in the drug release, ex-vivo permeation study and biological samples. The simultaneously developed HPLC method was linear over the concentration range from 100 ng/ml to 10000 ng/ml for both drugs. The coefficient of determination (R^2) was found to be more than 0.999 for both drugs. The initial optimization of the formulation was conducted using the QbD approach with the CUR, and the final optimized batch was formulated with Ce6 instead. The process of preparing a combined dual drug lipidic nanoparticles (DDLN) involved hot emulsification, followed by size reduction using probe sonication method. The optimized dual drug lipidic nanoparticle (DDLN) containing curcumin and chlorin e6 exhibited a particle size of less than 100 nm, and entrapment efficiency for both molecules were found to be less than 85%. The therapeutic efficacy of the developed formulation was tested on B16F10 and A431 cell lines via cytotoxicity evaluation, combination index, cellular uptake, nuclear staining, DNA fragmentation, ROS generation, apoptosis, and cell cycle assays under NIR irradiation (665 nm). The DDLN treatment exhibited an IC_{50} value that was approximately 4.2 fold lower compared to free CUR, free Ce6, and the combination of free Ce6 and free CUR (FCE+FCC), under NIR irradiation (665 nm) in B16F10 and A431 cell lines at 24 h. It indicated that the longer retention of DDLN intracellularly reaches optimum concentration to exert cytotoxic action. The cellular uptake analysis showed that both cell lines exhibited clear, brighter fluorescence in the cytoplasm and nuclei were observed in DDLN-treated cells, suggesting quick internalization of DDLN. The geometric mean fluorescence of DDLN treated with laser light cells from 1672.2 ± 34.22 to 3445.54 ± 16.27 from 1 to 4 h for the B16F10 cell, whereas the geometric mean fluorescence of free Ce6-treated cells was increased from 850.4 ± 20.7 to 1620.7 ± 23.67 . Similarly, the geometric mean fluorescence of DDLN (+ L) treated cells from 1752.32 ± 20.32 to 3945.54 ± 26.27 from 1 to 4 h for A431 cell lines. Co-delivering curcumin and chlorin e6 exhibited synergistic effects, higher cellular uptake, better cancer growth inhibition, and pronounced apoptotic events compared to the free drug-alone formulation. Our results depicted that topically applying this ROS generative dual drug-loaded lipidic nanoparticles incorporated in SEPINEO gel achieves better permeation (80 ± 2.45 %) across the skin and exhibited higher skin retention.

Dermatopharmacokinetic results of DDLN exhibited that the total concentration of CUR and Ce6 (DDLN gel) retained AUC_{0-32} skin in the epidermis and dermis layers was significantly high

compared to the FCE+FCC-gel. The total amount of concentration of CUR and Ce6 in the epidermis layer was increased with DDLN gel (CUR) ($711.32 \pm 39.02 \mu\text{g}/\text{cm}^2 \cdot \text{h}$) and for DDLN gel (Ce6) ($833.89 \pm 20.90 \mu\text{g}/\text{cm}^2 \cdot \text{h}$) in comparison to FCE+FCC-gel-CUR ($294.91 \pm 5.338 \mu\text{g}/\text{cm}^2 \cdot \text{h}$) and for FCE+FCC-gel-Ce6 ($277.50 \pm 4.202 \mu\text{g}/\text{cm}^2 \cdot \text{h}$). Dermatopharmacokinetic results stated that lipids-containing nanocarriers are efficient in intermingling with lipid bilayer membranes which results in lipid rearrangement that could exhibit higher permeation and higher residence time in the skin layers, which was confirmed with Confocal microscopy. This work puts forth photo-triggered ROS generative dual drug-based lipidic nanoparticles, which are simple and efficient to develop and exhibit synergistic therapeutic effects against cutaneous melanoma and basal cell carcinoma.



The specific aims laid to achieve the major objectives include

To achieve the aim of the thesis, the following objectives have been designed that were divided into different chapters focusing on each objective.

1. Design and characterization of itraconazole and chlorin e6 dual-drug loaded lipidic nanocarriers for skin cancer treatment

- i. Analytical method development and validation for the analysis of itraconazole (ITZ) and chlorin e6 (Ce6) by RP-HPLC and Spectrofluorometric techniques
- ii. Preparation and characterization of dual drug-loaded lipidic nanoparticles of itraconazole and Chlorin e6 (ITZ/Ce6@LNPs) by quality-by-design approach
- iii. Stability study of ITZ/Ce6@LNPs and ITZ/Ce6@LNPs Gel
- iv. In-vitro Cell Culture Studies
- v. Ex-vivo skin permeation studies
- vi. Ex vivo bioimaging in tumor skin of the C57BL/6 mice
- vii. Topical biodistribution study in C57BL/6 mice skin cancer model
- viii. In vivo antitumor efficacy study in C57BL/6 mice skin cancer model

2. Design and characterization of curcumin and chlorin e6 dual-drug loaded lipidic nanocarriers for skin cancer treatment

- i. Simultaneous analytical method development and validation for the analysis of curcumin (CUR) and chlorin e6 (Ce6) by RP-HPLC technique
- ii. Preparation and characterization of dual drug-loaded lipidic nanoparticles (DDLN) of curcumin and chlorin e6 (ITZ/Ce6@LNPs) by quality-by-design approach
- iii. Stability Study of DDLN and DDLN Gel
- iv. In-vitro Cell Culture Studies
- v. Ex-vivo skin permeation studies
- vi. Ex-vivo skin permeation studies by confocal microscopy
- vii. Dermatopharmacokinetic study of DDLN gel formulation

Introduction

There are various treatment options available for both multiple myeloma (MM) and non-melanoma skin cancer (NMSC), including both surgical and non-surgical procedures. These treatment modalities encompass a range of approaches to address these conditions. [1]. Photodynamic therapy (PDT) is a non-surgical treatment that demonstrates excellent efficacy in targeting a broad region, leading to favourable clinical results. Among these treatment approaches, topical chemotherapy is also a widely used treatment approach due to its cost-effectiveness and convenience. However, problems associated with the above treatment modalities have been the most common choice of treatment, but it has its own disadvantages. However, due to prolonged chemotherapy, and poor penetration of tumours, limited light penetration ability, cells develop drug resistance and, thus, result in unsuccessful therapy. PDT has demonstrated efficacy in the treatment of pre-malignant and malignant NMSC, according to several clinical research studies. However, challenges arise when tumors develop resistance, recurrence, or metastasis, sometimes becoming more aggressive. As a result, there has been a growing emphasis in MM and NMSC research on investigating the synergistic potential of combining photodynamic therapy (PDT) with other treatment modalities to augment its therapeutic efficacy.

Depending on the characteristics and type of the tumor, photodynamic therapy (PDT) can be employed in conjunction with immunomodulatory agents like Imiquimod, as well as chemotherapeutic agents such as 5-fluorouracil, methotrexate, or ingenol mebutate. This combination approach allows for a tailored treatment strategy based on the specific needs of the patient. Additionally, inhibitors targeting molecules involved in the carcinogenic process or pathways, such as COX2 or MAPK inhibitors and Sonic Hedgehog pathway inhibitors, along with surgical techniques and radiotherapy, have been explored as combinational approaches. These innovative approaches present optimistic paths towards improving the prevention and elimination of skin cancer [2]. Research has shown that the hedgehog pathway plays a role in the development of basal cell carcinoma (BCC) and melanoma. [3,4]. One specific mutation in the Hh pathway is responsible for 85% of BCC cases. The initial-stage drug prototype, Cyclopamine, exhibited encouraging results as a hedgehog pathway inhibitor in the treatment of skin cancer, particularly basal cell carcinoma (BCC). However, clinical application of cyclopamine was hindered by its limited solubility and associated toxicity, leading to ineffective results [5].

In recent times, the USFDA has granted approval for vismodegib and sonidegib, which are derived from cyclopamine, for oral administration in the treatment of skin cancer. These approvals signify a significant development in the therapeutic options available for managing skin cancer. However, studies have indicated that oral vismodegib and sonidegib may cause adverse effects such as muscle spasms, alopecia, and weight loss.[6]. Resistance to vismodegib is a significant challenge, primarily due to specific Smo mutations occurring at positions 473 and 477. These mutations result in the loss of vismodegib's binding capacity. The administration of oral formulations poses challenges for unconscious patients due to difficulties in ingestion, the inability to mask the taste, and the cumbersome nature of bulky formulations. As a result, topical administration of anti-cancer drugs has emerged as a preferable and effective option for treating skin cancer. Topical treatments offer better patient compliance, a crucial factor, especially for cancer patients. Currently, only 5-fluorouracil and imiquimod drugs are available in the market for topical skin cancer treatment. However, these drugs are associated with adverse effects such as skin irritation, hair loss, pain, and changes in skin colour. Additionally, the limited ability of these medications to deeply penetrate tissues or lesions, coupled with the restricted permeability of light, poses significant challenges in terms of drug absorption through the outermost layer of the skin (stratum corneum). Consequently, their efficacy in managing disseminated tumors is notably diminished. In addition, the lack of specific targeting to the desired site significantly diminishes the effectiveness of single-drug therapy in treating cancer. The new generation of photosensitizers, such as chlorin e6, HPPH, etc. can irradiate at deeper lesions or tissues because these agents get activated at near-infrared (NIR) region and show a high singlet oxygen quantum yield.

Itraconazole (ITZ), a potent antifungal agent, was recently shown to be efficient for the treatment of BCC in a clinical trial. It exerts its effects through multiple mechanisms to impede tumor growth. These mechanisms encompass the inhibition of the Hedgehog pathway, reduction in endothelial cell proliferation, induction of cell cycle arrest, and stimulation of autophagocytosis. [7]. Its primary action involves preventing the localization of SMO to the cilia, making it an effective inhibitor of the Hedgehog pathway and earning the designation of a ciliary translocation inhibitor. With an IC_{50} value of approximately 800 nM, it demonstrates potent inhibition of the Hh pathway. Furthermore, when administered orally, the systemic treatment provides sustained effects lasting for months.[6]. Itraconazole, when administered orally, exhibits a relatively weaker inhibition of the hedgehog (HH) pathway and has demonstrated evidence of reduced basal cell carcinomas (BCCs) in *Ptch1*^{+/-} mice as well as

in a phase 2 trial. In mice, itraconazole has shown its ability to inhibit the growth of human melanoma and improve survival. This effect is attributed to its capacity to suppress Hedgehog signaling. Nevertheless, long-term treatment with oral itraconazole carries potential risks, including the development of liver dysfunction and congestive heart failure. [8,9]. It effectively inhibited the Hh pathway and growth of BCC by directly binding with SMO. Studies indicate that ITZ has the capacity to inhibit tumors that have developed resistance to other hedgehog inhibitors, such as vismodegib. This is due to ITZ ability to bind to a distinct position on SMO (Smoothed protein), offering an alternative mechanism of action [10,11]. Furthermore, ITZ is highly effective against BCC when it is combined with PDT therapy.

To overcome these drawbacks, a novel lipid nanoparticle platform has been created, which utilizes charged-based squalene, enabling the co-delivery of chlorin e6 photosensitizer and Itraconazole. lipid nanocarriers have been explored as an alternative approach for topical drug delivery. It has many advantages for better permeation due to the interaction of carrier lipids molecules with stratum corneum. Modification of the charge in the lipidic nanocarriers is hypothesized to permeate the drug through the skin.

To the best our knowledge, there is no effective topical formulation available for skin delivery of combining of chlorin e6 and ITZ in skin cancer treatment, and therefore, it is required to develop combinational drug delivery for the inhibit the tumors that has shown the resistance to other hedgehog inhibitors like vismodegib. Co-delivery of Chlorin e6 photosensitizing agent and ITZ antifungal (repurposing molecules) has the potential to improve anti-tumor efficacy and reduce cancer resistance.

3.1. Materials and methods:

Curcumin was obtained from Himedia in Mumbai, India, while Chlorin e6 was purchased from Cayman Chemical Company in the United States. The following items were purchased from Himedia in Mumbai, India: Phosphate Buffered Saline (PBS) with a pH of 7.4, 3-(4,5-dimethylthiazol-2-yl)-2,5-diphenyltetrazolium bromide (MTT), heat-inactivated fetal bovine serum (FBS), trypsin-EDTA, Fluoromount-G, Penicillin-streptomycin antibiotic, Trypan blue solution, and Dulbecco's Modified Eagle Medium (DMEM). Precirol® ATO 5, Glyceryl monostearate (GMS), Compritol® 888 ATO, and stearic acid were generously provided by Gattefosse in Lyon, France. BASF India Ltd in Mumbai, India kindly provided Solutol HS 15, Tween 80, and Span 80 as gifts. Abitec Corporation, located in Ohio, USA, generously supplied Captex 355 and Capmul MCM C8 as gifts. Lipoid GmbH graciously provided DOTAP. Sigma-Aldrich in Bangalore, India supplied Dimethyl sulfoxide (DMSO), HPLC grade Methanol, paraformaldehyde, dichloro-dihydro-fluorescein diacetate (DCHF-DA), 4,6-diamidino-2-phenylindole (DAPI), 9,10-dimethyl anthracene (DMA), ethidium bromide, acridine orange (AO), N, N-Dimethyl-4-nitrosoaniline (RNO), and propidium iodide (Pi) for the research. Thermo Fisher Scientific in the USA provided the Singlet Oxygen Sensor Green (SOSG), while the GSure DNA genomic isolation kit was purchased from GCC Biotech Pvt Ltd in India. The Annexin-V-FITC apoptosis detection kit was obtained from R&D Systems, located in Minneapolis, USA.

Methods

titled "Design and Characterization of Itraconazole and Chlorin e6 Dual-Drug Loaded Lipidic Nanocarriers for Skin Cancer Treatment," we prepared dual drug-loaded lipidic nanoparticles (ITZ/Ce6@LNPs) using the QbD approach. These nanoparticles were characterized using various techniques, including particle size distribution, zeta potential, scanning electron microscopy, quantification of singlet oxygen generation, and percent cumulative drug release, etc. Moreover, we conducted in-vitro cell culture studies to further evaluate the nanoparticles. These studies involved cytotoxicity assays, cellular uptake studies, combination index analysis, assessment of mitochondrial membrane potential, analysis of nuclear morphology, in-vitro reactive oxygen generation assays, apoptosis assays, and cell cycle analysis, etc. Further, we loaded the developed nanoformulation (ITZ/Ce6@LNPs) into sepineo gel and subjected it to rheological characterization, ex-vivo permeation studies, and ex-vivo bioimaging in the tumor skin of C57BL/6 mice, etc. Additionally, we performed a topical biodistribution study on

tumor-bearing mice using an in vivo imaging system (IVIS). The developed formulation was further evaluated through an in-vivo antitumor efficacy study using a B16F10-induced mice skin cancer model.

In details procedure

3.1.1. Formulation of drug-loaded lipidic nanoparticles (LNPs)

To formulate lipidic nanoparticles loaded with the drug, the hot homogenization method was utilized, followed by probe sonication. Itraconazole (ITZ) was mixed with the liquid and solid lipid in a sterile vial and dissolved in methanol, which acted as the organic phase. Tween 20 and DOTAP were taken in another vial and vortexed for 10 minutes (aqueous phase). Both the vials were kept at constant heating at the same temperature (60°C) on a stirrer. Once the organic phase was fully evaporated from the lipid mixture, the aqueous phase was introduced to the oily phase. Subsequently, the resulting mixture was subjected to stirring for a duration of 5 minutes. Following that, the obtained pre-emulsion was subjected to sonication using a probe sonicator, and subsequently maintained at a low temperature to achieve the formation of lipidic nanoparticles (LNPs).

To eliminate the untrapped ITZ, the LNPs underwent centrifugation at 5000 rate per minute for 5 min. Afterward, the collected liquid portion above the sediment, known as the supernatant, was obtained. The Malvern Nano ZS instrument utilizing dynamic light scattering (DLS) was employed to measure the average particle size, polydispersity index (PDI), and zeta potential of the samples. The drug loading percentage and entrapment efficiency were computed using the provided formula and mathematical calculations. [12].

$$\text{Encapsulation efficiency (\%)} = \frac{\text{Amount of drug in the LNPs}}{\text{Initial amount of drug taken}} \times 100$$

$$\text{Drug loading (\%)} = \frac{\text{Amount of drug in the LNPs}}{\text{weight of LNPs}} \times 100$$

3.1.2. Optimization of drug loaded lipidic nanoparticle by using Box Behnken Design

To optimize the lipidic nanoparticles (LNPs), a Box-Behnken Design (BBD) was utilized with the assistance of Design-Expert software (Version V 13, Stat-Ease Inc., Minneapolis, MN,

U.S.A.). This design approach aimed to determine the optimal formulation with the minimum number of experiments needed. BBD allows for the evaluation of interaction effects between critical process parameters and materials attributes. The solid and liquid lipids, surfactant concentration, and probe sonication time were determined at three levels based on preliminary batches of LPNs. The independent variables were varied within ranges of solid lipid: liquid lipid ratio (X1) from 100 to 200 mg, surfactant concentration (X2) from 2 to 6 %, and probe sonication time (X3) from 2 to 6 min. To assess the reproducibility of the design, five centre points were used. The software generated 17 runs with high, medium, and low levels. The suggested experiments were carried out and the experimental data were included in the Design of the experiment software. A statistical analysis was carried out to determine the regression model that provides the best fit for each response variable. The model selection was based on the inclusion of significant additional terms, non-aliased models, and the highest-order polynomial. To determine the most appropriate model, an analysis of variance (ANOVA) was conducted for all the response variables. During the evaluation process, multiple criteria were utilized, including the multiple correlation coefficient (R²), adjusted and predicted correlation coefficients, standard deviation, and coefficient of variance. Design-Expert software was utilized to generate numerical and graphical data, including 3D response surface plots and 2D counterplots, to visualize the experimental results. The generated visualizations were employed to examine the interaction effects between the independent and dependent variables. The main focus of model optimization was to attain the smallest particle size and the highest percentage of entrapment efficiency. The final optimized batch was validated by comparing predicted values to experimental batch results in terms of percent variation or error. The BBD model was validated quantitatively in this manner

3.1.3. Preparation and characterization of dual drug-loaded lipidic nanoparticles of ITZ and Ce6 (ITZ/Ce6@LNPs)

After optimizing the validated batch, we formulated a final formulation batch (ITZ/Ce6@LNPs) by combining precirol ATO (145 mg), Squalene (50 mg), chlorin e6 (5 mg), and ITZ (5 mg) and Span 80 (200 mg) in a vial (Organic phase). We added 200 µl of methanol ACN mixture and 10 µl of DMSO to the vial as an organic solvent to dissolve the ingredients. In a separate vial, we mixed and continuously vortexed tween 20 (200 mg) and DOTAP phospholipid for 10 minutes before adding the solubilized component to the water phase. We then followed the same methodology protocol as discussed earlier to further treat the formulation. To determine the % EE and drug loading of the ITZ from the ITZ/Ce6@LNPs.

The samples were analyzed using high-performance liquid chromatography (HPLC) at a wavelength of 271 nm to estimate their properties. In order to assess the entrapment efficiency of chlorin e6 in ITZ/Ce6@LNP, we developed and validated a fluorescence spectroscopy method specifically for chlorin e6 using spectrofluorolog.

3.1.4. Physiochemical Characterization of ITZ/Ce6@LNPs

To determine the morphology of the developed ITZ/Ce6@LNPs, we utilized Field Emission-Scanning Electron Microscopy (FE-SEM) and scanning transmission electron microscopy. The FE-SEM equipment used was the FEI Quanta FEG 250 SEM.

3.1.4.1. Morphological analysis

To determine the surface morphology of the ITZ/Ce6@LNPs, Scanning Electron Microscopy (SEM) was used with a NOVA NANOSEM 450 with the inclusion of a cryoprotectant (mannitol). During the sample preparation, a consistent layer of ITZ/Ce6@LNPs was applied onto adhesive carbon tape, which was securely attached to aluminum stubs followed by the gold coating under 20 kV for further examination.

3.1.4.2. Spectroscopic analysis

UV spectroscopy on free ITZ, free Ce6, and ITZ/Ce6@LNPs was performed using the Jasco UV-670 Spectrophotometer from the United States. [13]. In order to verify the encapsulation of both drugs, the ITZ/Ce6@LNPs were dissolved in ethanol, and their UV spectrum was obtained and compared.

3.1.4.3. Kinetic stability

The stability of the dual drug-loaded ITZ/Ce6@LNPs was assessed by storing it at 4°C for 24 days, during which the drug absorbance was monitored for the first six days using a UV instrument.

3.1.4.4. Evaluation of singlet oxygen generation (SOG)

This study aimed to evaluate the production of singlet oxygen ($^1\text{O}_2$) by ITZ, Ce6, and ITZ/Ce6@LNPs. To measure $^1\text{O}_2$ generation, a fluorescent dye called 9,10-dimethyl anthracene (DMA) was utilized. Ce6-containing formulations (1.5 μg) were dissolved in 1 ml of DMSO and Phosphate buffer Saline pH 7.4. Subsequently, DMA (20 mM) was added to the mixture. After a 10-minute equilibration period, the mixture was exposed to a laser source (660 nm) at an intensity of 0.5 W/cm² for various durations. [14]. Fluorescence intensity

measurements of DMA were conducted using a microplate reader at excitation and emission wavelengths of 360 nm and 380-550 nm, respectively. These measurements aimed to quantify the reduction in fluorescence intensity. [15].

To assess the production of singlet oxygen (1O_2) by ITZ/Ce6@LNPs, free ITZ, and free Ce6, a singlet oxygen indicator called N,N-dimethyl-4-nitrosoaniline (RNO) was utilized in combination with histidine, which serves as a 1O_2 trap. The free drugs and ITZ/Ce6@LNPs were mixed with an aqueous solution containing 100 μ l of RNO (250 mM) and 300 μ l of histidine (30 mM). Subsequently, the resulting mixture (200 μ l) was added to a 96-well plate and exposed to a laser source with a wavelength of 660 nm and an intensity of 0.5 W/cm². The absorbance of RNO at 440 nm (λ_{max}) was measured using a UV-vis microplate reader at specific time intervals during the irradiation process. [16].

The singlet oxygen sensor green (SOSG) was utilized to determine the presence of singlet oxygen (1O_2) in the ITZ, Ce6, and ITZ/Ce6@LNPs in their free forms. This involved dissolving the ITZ/Ce6@LNPs at a specific concentration with 0.25 μ M of Ce6 in PBS pH 7.4. The mixture was then combined with 2.5 μ M of SOSG. Subsequently, all samples were exposed to a laser source with a wavelength of 660 nm (λ_{max}). The singlet oxygen sensor green (SOSG) fluorescence intensity was measured at excitation and emission wavelengths of 494 nm and 534 nm, respectively, following the irradiation process. [17].

3.1.4.5. In-vitro drug release analysis

To evaluate the in-vitro release of ITZ/Ce6@LNPs, free ITZ, and free Ce6, the dialysis bag method was employed using a buffer system that mimicked skin conditions. The buffer consisted of 15% ethanol, 2% Tween 80, and pH 6.4 phosphate buffer saline, which provided stability and a sink condition for ITZ+Ce6. For the experiment, a dialysis bag with a molecular weight cutoff of 12 KDa (Himedia) was filled with the ITZ/Ce6@LNPs formulation (equivalent to 0.1 mg of ITZ and Ce6 in 1 ml, n = 3) as well as the pure drug formulation (ITZ+Ce6). The bag was then placed in 30 ml of the aforementioned release medium. The samples were incubated at 32 °C in a shaking incubator at 200 rpm. At specific time intervals (0.5, 1, 2, 4, 6, 8, 12, and 24 h), 1 ml aliquots were collected, and an equal volume of fresh release medium was added back to the dialysis bag. The collected samples were filtered and analyzed using an HPLC method to quantify ITZ levels. Simultaneously, the samples were analyzed by fluorescence spectroscopy method to determine the concentration of Ce6.

Various kinetic models, such as zero order, first order, Higuchi, and Korsmeyer-Peppas, were assessed using the DD solver program (Excel add-in), and the most appropriate model was chosen based on the highest correlation coefficients (R^2).

3.1.5. Preparation and characterization of an ITZ/Ce6@LNPs Gel

To formulate the gel containing ITZ/Ce6@LNPs, SEPINEOTM P 600 was used as the gel-forming agent at a concentration equivalent to 0.05% w/w of ITZ and Ce6 (10 g). SEPINEOTM P 600 consists of acrylamide/sodium Acryloyl dimethyl/Taurate copolymer/isohehexadecane & polysorbate 80. The gel preparation involved adding 2% w/w of SEPINEOTM P 600 to a beaker, followed by the addition of freshly prepared ITZ/Ce6@LNPs. Gentle stirring was applied to ensure a homogeneous gel consistency. The final ITZ/Ce6@LNPs gel was characterized by examining its pH, spreadability, and morphology using a scanning electron microscope (SEM).

3.1.5.1. Rheological behaviour and stability of ITZ/Ce6@LNPs Gel

3.1.5.1.1. Simple Viscosity

The Rheological and flow properties of the ITZ/Ce6@LNPs gel were analyzed using a Rheometer (MCR 92, P-PTD 200, Anton Paar, Germany). To determine the viscosity of the gel, a parallel plate (PP-25 mm diameter) with a 0.2 mm gap between the plate and probe was utilized. The shear rate was maintained at 10 s⁻¹ for a duration of 5 minutes, and a total of 30 data points were recorded to calculate the viscosity in cP (centipoise). [18].

3.1.5.1.2. Temperature-dependent viscosity

To investigate the thermal properties of the gel, temperature-dependent viscosity analysis was conducted. This test aimed to observe the gel's behavior when subjected to different temperatures. The experiment involved using a parallel plate (PP-25 mm diameter) with a 0.2 mm gap between the container and probe. The optimized sample of ITZ/Ce6@LNPs Gel (500 mg) was loaded onto the plate, and the temperature was gradually increased from 25°C to 40°C. The heating rate was set at 1°C per minute, and a total of 30 data points were recorded during the experiment.

3.1.5.1.3. Amplitude sweeps test and Frequency sweeps test

The amplitude sweep test is a commonly used method to evaluate the characteristics of gels, dispersions, and pastes. It helps determine the linear viscoelastic region (LVE), which represents the range where the sample structure remains unchanged. The yield point estimation measures the critical stress at which gels or dispersed materials start to flow, indicating the force required to initiate gel flow.

In this study, the optimized sample of ITZ/Ce6@LNPs (500 mg) was loaded onto the plate at a temperature of 25°C. To determine the storage modulus (G') and loss modulus (G''), the shear strain γ was systematically varied from 0.01% to 1% at a frequency rate of 10 rad/sec. The frequency sweep test was conducted to examine the internal structure and long-term stability of the gel dispersion. It provides information on the time-dependent behavior of the gel within the range of non-destructive deformation. The ITZ/Ce6@LNPs gel was subjected to an angular frequency range of 0.1 to 100 rad/s, and parameters such as G' , G'' , and complex viscosity were evaluated. [19].

3.1.5.2. Stability study of ITZ/Ce6@LNPs and ITZ/Ce6@LNPs Gel

The stability of the developed ITZ/Ce6@LNPs formulations and ITZ/Ce6@LNPs gel was investigated for a period of 90 days at temperatures of 2-8 °C and 32 °C. The average particle size of ITZ/Ce6@LNPs was determined using the Malvern Nano ZS instrument, while the entrapment efficiency was calculated using a similar formula as mentioned before. To assess the stability of the ITZ/Ce6@LNPs gel, the drug content (assay) was analyzed. A 100 mg sample of the gel was mixed with a solvent combination of ACN and methanol (1:1 ratio) in microcentrifuge tubes. The mixture was sonicated in a bath for 5 minutes to extract the drugs. Subsequently, the samples were centrifuged at 12000 RPM for 15 minutes, and the resulting supernatant was analyzed using both RP-HPLC method and fluorescence spectroscopy to determine the drug content. This stability evaluation aimed to determine the performance of the formulations over the designated timeframe and under different storage conditions.

3.1.5.3. Texture analysis

The textural properties of the ITZ/Ce6@LNPs gel formulation, including firmness and adherence, were evaluated using the TA-XT2 Texture AnalyzerTM. This analysis aimed to study the gel's textural profile. To perform the analysis, the prepared ITZ/Ce6@LNPs gel was transferred to a glass beaker with a capacity of 100 ml. The gel was filled up to the 70 ml mark to prevent the formation of air bubbles and ensure a flat surface. The analytical probe was then used to compress the gel at a rate of 2 mm/s to a depth of 30 mm. The regulated texture analyzer

software was employed to obtain various texture parameters such as firmness, cohesiveness, and consistency. Through this analysis, the texture analyzer provided insights into the physical properties of the ITZ/Ce6@LNPs gel, helping to characterize its firmness, adherence, and other relevant textural attributes.

3.1.6. In-vitro cell culture studies

3.1.6.1. Cellular uptake studies

The cell uptake of Ce6 and ITZ/Ce6@LNPs by B16F10 and A431 cells was evaluated through quantitative and qualitative methods. In brief B16F10 and A431 cells (50,000 cells each) were seeded in 12-well plates followed by incubation overnight at 37°C. The media was then replaced with fresh media containing Ce6 and ITZ/Ce6@LNPs at a concentration of 6 µg/ml of Ce6, followed by further incubation at 37°C for varying durations (1 to 4 h). For quantitative analysis using flow cytometry, the cells were treated similarly, washed with PBS 7.4, trypsinized, and centrifuged to collect the cell pellet. The cells were then washed and resuspended in PBS 7.4. The fluorescence intensity of 10,000 viable cells was measured using a flow cytometer. The acquired data was processed using FACS DIVA Software. Qualitative observations of cellular internalization were also conducted using a fluorescence microscope. After removing the media, the cells were washed with cold PBS, followed by fixed with 4% paraformaldehyde and stained with DAPI. Subsequently, the cells were rinsed with PBS and examined under a fluorescence microscope (Leica, Germany) to visualize the internalization at 1 and 4 h. This combined approach allowed for both quantitative and qualitative assessment of the uptake of Ce6 and ITZ/Ce6@LNPs by B16F10 and A431 cells, providing valuable insights into the cellular interactions of these compounds.

3.1.6.2. Cell viability assay

In this study, in vitro cell experiments were performed using two cell lines: B16F10, representing adherent murine melanoma cells, and A431, representing epidermoid carcinoma cells. To evaluate cytotoxicity, B16F10 and A431 cells were seeded in 96-well plates at a density of 10,000 cells per well and allowed to adhere for 24 h. Subsequently, various doses of ITZ, Ce6, ITZ + Ce6, and ITZ/Ce6@LNPs were added to the cells, ranging from 3.125 to 100 µg/ml, and incubated for 24 and 48 h. After a 12 h treatment period, the cells in the 96-well plates were subjected to NIR laser radiation at 666 nm (\pm L with light and without light, 0.5 W/cm²) for 5 minutes, followed by an additional 12 h incubation. Following incubation, the culture media was removed, and 50 µl of MTT solution in DMEM was added to each well.

The cells were further incubated in the dark for 4 h. Subsequently, the MTT solution was replaced with 150 µl of DMSO to dissolve the formazan crystals in each well. The absorbance of the samples was measured at wavelengths of 570 nm and 620 nm using a Spectramax™ multiplate reader (Molecular Devices, US). The following formula was used for quantification:

$$\text{Cell viability \%} = \frac{\text{Absorbance of sample}}{\text{Absorbance of control}} \times 100$$

The software GraphPad Prism 9.0.2 was utilized to calculate the IC₅₀ value. After conducting the experiments in triplicate, the results obtained from each test were averaged.

3.1.6.3. Combination index analysis

The synergy of the drug combinations was quantified using the Chou-Talalay method. The IC₁₀ to IC₉₀ values of the free drugs, combinations, and prepared formulations were calculated using GraphPad Prism. To assess the combination index (CI) and develop a graph correlating the CI with the fraction affected (Fa), CompuSyn Software was utilized. The CI value indicates the nature of the drug interaction: a value less than one indicates synergistic effects, a value equal to one indicates additive effects, and a value greater than one indicates antagonistic effects. [20].

$$CI_x = \frac{D_1}{A_1} + \frac{D_2}{A_2}$$

Where A₁: a dose of drug 1 to produce x% cell kill alone;

D₁: a dose of drug 1 to produce x % cell kill in combination with (D)₂;

A₂: a dose of drug 2 to produce x % cell kill alone;

D₂: a dose of drug 2 to produce x % cell kill in combination with (D)₁

3.1.6.4. Annexin V assay

To determine apoptosis induced by ITZ, Ce6, ITZ + Ce6, and ITZ/Ce6@LNPs in B16F10 and A431 cells, the TACS® Annexin V-FITC Kit was utilized. The cells were cultured in 12-well plates and treated with the respective compounds for 12 h at a constant Ce6 concentration of 10 µg/ml. Subsequently, the cells were exposed to a 666 nm NIR laser for 5 minutes at a power density of 0.5 W/cm². After thorough washing with PBS buffer, the cells were trypsinized and

suspended in 1X binding buffer. Annexin V-FITC conjugate was added to each cell suspension and incubated at room temperature for 10 minutes, protected from light. Following this, the cells were treated with propidium iodide (PI) solution at a concentration of 1 $\mu\text{g/ml}$ for 5 minutes. The samples were then analyzed using a flow cytometer. Apoptotic cells were identified by their exclusive staining with Annexin V-FITC conjugate within a gated cell population, enabling the determination of the percentage of apoptotic cells.

3.1.6.5. Cell cycle analysis

Cell-cycle analysis and the distribution of cells in the various phases such as S, G₀/G₁, and G₂/M were performed using flow cytometry. The cells (B16F10 and A431) were cultured and maintained in 12-well plates as mentioned earlier. They were then treated with ITZ, Ce6, ITZ + Ce6, or ITZ/Ce6@LNPs, with or without 666 nm NIR laser radiation, and incubated for 12 h at a fixed Ce6 concentration of 10 $\mu\text{g/ml}$. After treatment, the cells were trypsinized, centrifuged, washed with 1X PBS, and centrifuged again. The cell samples were fixed with chilled ethanol and stored at -20 °C for 3 h. They were then centrifuged and rinsed with 1X PBS. Each sample was treated with RNase and incubated for 15 minutes. Subsequently, PI solution was added from the 1mM stock solution, and the samples were kept for incubation in the dark condition for 20 minutes. Flow cytometry analysis was performed using a flow cytometer system (BD Biosciences, USA).

3.1.6.6. Mitochondrial membrane potential (MMP) Study

The disruption of mitochondrial membrane potential ($\Delta\Psi\text{m}$) can serve as an indicator of cellular stress and early apoptosis. To assess $\Delta\Psi\text{m}$, the JC-1 dye was employed, which can reversibly form clusters in the mitochondrial membrane based on its potential. At low $\Delta\Psi\text{m}$, JC-1 exists as j-monomers, emitting green fluorescence in the cytosol at 530 nm. At higher $\Delta\Psi\text{m}$, it forms j-aggregate complexes, resulting in red fluorescence in the mitochondrial membrane. The ratio of green-to-red fluorescence emission indicates the extent of mitochondrial membrane depolarization, making JC-1 a valuable marker for early apoptosis. To investigate this phenomenon, B16F10 and A431 cells were separately treated with ITZ, Ce6, ITZ + Ce6, or ITZ/Ce6@LNPs at their respective IC₅₀ concentrations. Subsequently, the cells were exposed to NIR laser radiation at 666 nm (1 W/cm²) for 5 minutes. After 24 h, the cells were trypsinized, centrifuged, washed with PBS, and stained with JC-1 dye (2 μM) for 15 minutes. Quantitative analysis was performed using a flow cytometer (BD FACS Area III) with

excitation at 485 nm and emission at 590 nm, applying appropriate compensation and threshold settings. Qualitative analysis was conducted using a fluorescence microscope to capture images for further examination. [21].

3.1.6.7. Reactive oxygen species (ROS) assay

To assess the production of reactive oxygen species (ROS) in B16F10 and A431 cells, the redox-sensitive fluorogenic probe 2',7'-dichlorodihydrofluorescein diacetate (DCF-DA) was employed. After treatment with ITZ, Ce6, ITZ + Ce6, or ITZ/Ce6@LNPs, the cells were exposed to light source (NIR laser radiation at 666 nm (\pm L) for 5 minutes). DCF-DA, which is initially non-fluorescent, undergoes intracellular transformation and oxidation mediated by esterases to generate the highly fluorescent compound as 2',7'-dichlorofluorescein (DCF). For the experimental procedure, B16F10 and A431 cells were cultured in 12-well plates and treated separately with ITZ, Ce6, ITZ + Ce6, or ITZ/Ce6@LNPs at a constant Ce6 concentration of 10 μ g/ml for 24 h. After treatment, the cells were rinsed with PBS and subjected to incubation with DCF-DA dye at 37°C for a duration of 30 minutes. Subsequently, the cells were labeled with DAPI and images were captured using a fluorescence microscope (green channel). The fluorescence excitation was set at 492-495 nm, and emission was recorded at 517-527 nm.

3.1.6.8. Nuclear staining assay

To examine nuclear morphological changes, DAPI staining was conducted on B16F10 and A431 cells treated with ITZ, Ce6, ITZ + Ce6, or ITZ/Ce6@LNPs, with or without exposure to NIR laser radiation at 666 nm. DAPI is a fluorescent dye that specifically binds to DNA regions rich in adenine-thymine base pairs, enabling visualization of both live and fixed cells. For the experimental procedure, approximately 1×10^5 A431 and B16F10 cells were cultured in a 12-well plate. The cells were treated with ITZ, Ce6, ITZ + Ce6, or ITZ/Ce6@LNPs for a duration of 24 h. Following the incubation period, the cells were washed with PBS, fixed with 4% paraformaldehyde for 20 minutes at 37 °C, and stained with DAPI (10 μ l, 0.5 μ g/ml) for 5 minutes. Additionally, acridine orange (AO) staining (0.1 mg/ml) was performed for 20 minutes. After another PBS wash to remove excess stain, the cells were visualized using a fluorescence microscope (Leica, Germany) with emission in the green channel (AO, 480-490 nm) and the blue channel (DAPI, 358 nm).

3.1.6.9. DNA fragmentation

A431 and B16F10 cell lines were seeded in a 6-well tissue culture plate at a density of 5×10^4 cells per well and allowed to grow overnight. The cells were then treated with free ITZ, free Ce6, ITZ + Ce6, and ITZ/Ce6@LNPs at a Ce6 concentration of $10 \mu\text{g/ml}$, followed by a 12 h incubation period at 37°C . After the incubation, the cells were exposed to a 660 nm laser at a power density of 0.5 W/cm^2 for 5 minutes. Subsequently, they were incubated for an additional 12 h at 37°C . Upon completion of the treatment period, the cells were collected, and DNA extraction was carried out using GSure DNA genomic isolation kits. The purity of the isolated DNA was assessed by measuring the absorbance at 260 nm and 280 nm. The extracted DNA samples were then loaded onto a 1.5% agarose gel containing ethidium bromide dye at a concentration of $0.5 \mu\text{g/ml}$. Visualization of the gel was performed using a Fusion Pulse GelDoc system (Vilber, Germany), and the degree of DNA fragmentation was observed under a microscope.

3.1.7. Ex-vivo and in vivo assessment of ITZ/Ce6@LNPs Gel

3.1.7.1. Ex-vivo skin permeation studies

Using a vertical Franz diffusion cell, ex vivo of ITZ/Ce6@LNPs gel (0.05 % w/w) penetration through the whole thickness of goat skin was assessed. The fresh goat ear skin was taken from the butcher shop. The subcutaneous fat and hair were removed, and the skin was properly cleaned three times with PBS. A vertical Franz diffusion cell was used to mount the processed skin, and 15 % ethanol, 2 % Tween 80, and 6.4 pH phosphate buffer solvent system were used in the receptor compartment. The volume of the receptor compartment was 18 ml with a surface area of 1.17 cm^2 . Prior to the experiment, the processed skin was kept for 2 h for hydration. Then 100 mg of the plane gel (ITZ+Ce6) and 100 mg of the ITZ/Ce6@LNPs gel formulation were applied to the donor compartment. The entire system was maintained at 200 rpm on a magnetic stirrer at $32 \pm 0.5^\circ\text{C}$. 1 ml of aliquot was collected, followed by replacement of the same volume with fresh release media at time intervals *viz.* 0.5 h, 1h, 2h, 4h, 6h, 8h, 12h, 24h. The collected sample was filtered through the $0.44 \mu\text{m}$ syringe filter and analyzed by using the in-house developed and validated RP-HPLC and Fluorescence spectroscopy. After analysing the results, a graph was constructed with time on the x-axis and the % cumulative ITZ/Ce6@LNPs permeate on the y-axis. Further, steady-state flow and lag time was calculated, and the slope of the graph gives the permeation flux ($\mu\text{g/cm}^2$) [22].

3.1.7.2. Establishment of B16F10 cells induced skin cancer model in C57 BL/6 mice.

In vivo studies using B16F10 cells have demonstrated their ability to form tumors in mice that closely resemble human melanoma tumors. These tumors exhibit key characteristics of cancer, including uncontrolled proliferation, angiogenesis, and invasion into surrounding tissues. The animal experiments conducted under protocols BITS-Hyd/IAEC/2022/57 were approved by the Institutional Animal Ethics Committee (IAEC) and followed the guidelines set forth by the CPCSEA. The animals were housed in standard plastic cages under laboratory conditions and allowed to acclimate for one week prior to the start of the experiments. A 12 h light and 12 h dark cycle was maintained for the animals. Tumors were induced by injecting 100 μ l of B16F10 cells, at a concentration of 1.5 million cells, into the right flank of female C57 mice under anaesthesia. Subsequently, the mice were divided into five groups, with each group consisting of five mice: control (PBS/Free gel), free Ce6, free ITZ, ITZ+Ce6, and ITZ/Ce6@LNPs gel.

3.1.7.3. Ex vivo bioimaging in tumor skin of the C57BL/6 mice

The distribution of ITZ/Ce6@LNPs in the tumor skin of C57BL/6 mice was examined using an ex-vivo approach. Here Ce6 acts as a fluorescence marker. The superficial tumor skin of C57BL/6 mice was obtained and placed between the donor and receptor compartments of Franz diffusion cells, securely held in place by clamps. The receptor compartment was filled with 18 ml of PBS (pH 6.4) containing 15% ethanol and 2% Tween 80, while the donor compartment contained either the free drug formulation gel (ITZ+Ce6) or the ITZ/Ce6@LNPs gel, equivalent to 100 μ g of Ce6. The skin samples were incubated for specific time intervals of 6, 12, and 24 h at a temperature of $37 \pm 1^\circ\text{C}$ with stirring at 800 rpm. At each designated time point, the skin samples were carefully washed, air-dried, and subjected to tape-stripping using 19 mm Scotch cellophane tape in order to remove the outermost layer of the skin, known as the stratum corneum. The remaining skin was then analyzed using ex-vivo bioimaging techniques. The imaging process involved using an In Vivo Imaging System (IVIS) with excitation and emission wavelengths set at 405 nm and 665 nm, respectively. This allowed for the visualization and quantification of the distribution of ITZ/Ce6@LNPs within the tumor skin samples.

3.1.7.4. Topical biodistribution study in C57BL/6 mice skin cancer model

In order to evaluate the in vivo topical biodistribution using imaging (, mice with B16F10 tumors (approximately 50 mm³) were treated topically with either 200 mg of free drug formulation gel (ITZ+Ce6) or ITZ/Ce6@LNPs gel (equivalent to 100 µg of Ce6). The mice were anesthetized and monitored using an IVIS in vivo imaging system at different intervals (1, 3, 6, 12, 24, and 48 h) after topical application. Furthermore, at 48 h post-treatment, mice were euthanized to examine nanoparticle distribution in the main organs, including the heart, liver, spleen, lung, kidney, and tumor, using IVIS imaging.

3.1.7.5. In Vivo antitumor efficacy

Once the tumors reached a size of approximately 50 mm³, the mice carrying the tumors were separated into five groups: PBS, free ITZ, free Ce6, ITZ+Ce6, and ITZ/Ce6@LNPs gel. The treatment doses for ITZ and Ce6 were 2.5 mg/kg each. A total of 200 mg of gel was topically applied to the tumor area on a regular basis for 8 days. After a post-application period of 12 h, the mice bearing B16F10 tumors were subjected to light irradiation (NIR laser radiation at 666 nm, with a power of 0.5 W/cm²) for 5 minutes. Throughout the treatment period, body weight and tumor growth rate were observed by measuring the perpendicular diameter using calipers. The volume of each tumor was calculated using the equation: tumor volume = (length × width²)/2. At the conclusion of the treatment period, the mice were sacrificed, and major organs, such as the heart, liver, spleen, lung, and kidney, along with the tumors, were excised for histological examination. Hematoxylin and eosin (H&E) staining, imaging, and immunohistochemistry were performed to assess the tissue samples.

3.1.7.6. Immunohistochemistry

3.1.7.6.1. Apoptosis assay by TUNEL assay

To evaluate the apoptotic effect, the TUNEL assay was applied on frozen tumor sections following the manufacturer's instructions. The tumor cryo-sections, with a thickness of 5 µm, were obtained using a cryotome (Leica). These sections were then fixed in a solution containing 4% paraformaldehyde for 10 minutes at room temperature. The FragEL™ DNA Fragmentation Detection Kit was employed for the TUNEL test, which detects DNA fragmentation in apoptotic cells. The tumor sections were subjected to the TUNEL assay according to the manufacturer's instructions. The presence of apoptotic cells, exhibiting green fluorescence, was observed, while the cell nuclei were stained with blue fluorescence. Images of the tumor slices were captured using a fluorescent microscope and enabling visualization and examination of the apoptotic cells.

3.1.7.6.2. Immuno-histochemical analysis for hematoxylin & eosin staining and Ki-67

Hematoxylin and eosin (H&E) staining is a commonly used method to examine the morphology of tissues that have undergone preservation, processing, embedding, and sectioning. Following eight days of treatment with different substances, including control (PBS), free Ce6, ITZ, ITZ+Ce6, and ITZ/Ce6/LNPs gel, the mice were euthanized. The heart, kidney, spleen, lung, liver, and tumor were isolated and fixed in a solution containing 4% paraformaldehyde. These tissue samples were then embedded in paraffin and subjected to H&E staining to assess potential organ toxicity and evaluate apoptosis of cancer cells. To assess cell proliferation within the tumor, immunohistochemistry analysis was performed using Ki67 staining. Ki67 is a nuclear antigen expressed during active phases of the cell cycle (M, G2, S, and G1), except during the resting phase (G0), making it a valuable marker for measuring cell proliferation. For the Ki67 analysis, slices of the tumor cryo-sections were incubated with a diluted solution of Ki67 antibody at a temperature of 4 °C. Subsequently, the slices were washed with PBS and treated with a secondary antibody labeled with Alexa Fluor® 488 for a duration of 2 h. Following that, the tissue slices were washed again with PBS and observed under a fluorescence microscope. This allowed for the visualization and analysis of the Ki67-stained cells within the tumor tissue.

3.1.7.7. ROS Production in tumor tissues

To assess the activity of reactive oxygen species (ROS) in tumor tissue, an experiment was conducted in mice. Initially, ITZ+Ce6 and ITZ/Ce6@LNPs were topically applied to the tumor area. After 24 h, a 50 µl intratumoral injection of DCFH-DA (25 µM) was administered. Following a 30-minute incubation period, the mice were anesthetized and observed using an in-vivo imaging system (IVIS® Lumina III, PerkinElmer, USA). Subsequently, the tumors were dissected and sectioned into 5 µm thick slices using a cryostat (Leica Biosystems, Germany). These tissue sections were stained with DAPI, mounted on glass slides, and examined under a fluorescence microscope (Leica, Germany) to visualize the fluorescence signals.

3.1.7.8. Statistics analysis

The findings of each test were performed in triplicate and are presented as mean and standard deviation (mean SD). The t-test and one-way ANOVA were performed to evaluate the significance of differences between all groups using GraphPad Prism software. When P values less than 0.05, the analysis was statistically significant. P values of 0.05, 0.01, and 0.001 are denoted by the *, **, and ***, respectively.

3.2. Results and discussion

The development of optimized lipidic nanoparticles (LNPs) using the QbD methodology and design of experiments involved statistically adjusting process parameters and material attributes to obtain the optimal batch with the fewest possible trials. We utilized BBD to optimize formulation with a 17-trial batch (3 factors and 3 levels) using Design-Expert 13.0 software from State-Ease Inc., Minneapolis, USA. The lipidic nanocarrier system was prepared using low-temperature homogenization followed by the probe sonication method, with the concentration of lipid (oil phase) and surfactant (aqueous phase) being the main factors affecting particle size and percentage entrapment efficiency. Three levels (low, medium, and high) of independent variables were selected (**Table 3.1**), and the results are presented in **Table 3.2**. The interactions between the independent variables and their responses were described using polynomial equations generated by the software. ANOVA was used to assess the validation of these equations (**Table 3.3**), and response surface plots were generated to study the interaction effect between responses such as percentage entrapment efficiency and particle size. The polynomial equations and surface plots helped to understand the effect of each variable individually and in combination with other variables on each response. Using response surface regression, full quadratic model equations for particle size and entrapment efficiency were obtained using Design-Expert software and are presented in **Table 3.4**.

Table 3.1. Levels of independent factors used in the design.

Variables		Selected CMAs and CPPs	Goal	Lower level (-1)	Middle level (0)	Upper level (+1)
Independent variables	X1	Amount of lipid (mg)	In range	100	150	200
	X2	Surfactant concentration (%)	In range	2	4	6
	X3	Probe sonication time (min)	In range	2	4	6
Dependent variables	Y1	Particle size (nm)	Minimum (80-100)			
	Y2	Entrapment efficiency (%)	Maximum (> 50 %)			

The regression equation includes the input variables A (lipid amount in mg), B (surfactant concentration in %), and C (probe sonication time in min), where a (+) positive sign indicates a positive quantifiable relationship between the input variable and the response value, while a (-) negative sign indicates an adversarial effect, resulting in a decrease in response value with the respective input variable. The analysis of the coefficient of equations and response surface plots (**Figure 3.1**) indicates that the particle size and entrapment efficiency are significantly dependent on the independent factors of lipid amount, surfactant concentration, and probe sonication time.

Table 3.2. The design of experiments executed for optimization of lipidic nanoparticles.

Batch No.	Independent variables			Response variables	
	Lipid (mg)	Surfactant (%)	Sonication (min)	Size (nm)	Entrapment Efficiency (%)
1	100	4	2	92.957 \pm 1.65	56.458 \pm 2.45
2	150	2	6	136.589 \pm 5.18	72.943 \pm 1.73
3	150	4	4	120.687 \pm 0.63	73.121 \pm 1.00
4	150	2	2	147.985 \pm 2.06	57.477 \pm 1.21
5	150	6	2	168.173 \pm 2.69	63.245 \pm 2.52
6	200	4	2	193.167 \pm 2.21	75.280 \pm 0.99
7	150	4	4	121.610 \pm 1.53	75.248 \pm 1.15
8	100	4	6	88.686 \pm 1.21	65.418 \pm 2.15
9	150	4	4	116.806 \pm 1.33	76.055 \pm 2.03
10	150	6	6	142.273 \pm 1.96	75.477 \pm 1.83
11	100	6	4	81.068 \pm 1.27	65.688 \pm 2.58
12	200	6	4	188.933 \pm 0.49	87.216 \pm 0.96
13	150	4	4	114.913 \pm 1.49	74.379 \pm 1.03
14	100	2	4	102.367 \pm 1.88	57.955 \pm 1.65
15	150	4	4	120.125 \pm 1.18	77.047 \pm 2.52
16	200	2	4	152.533 \pm 2.45	78.063 \pm 0.58
17	200	4	6	162.248 \pm 1.01	86.707 \pm 0.57

Table 3.3. ANOVA for regression coefficients for Box Behnken designed effects (linear, quadratic, and interaction) against the CQAs i.e., dependent variables (particle size and entrapment efficiency) to establish the best fitted quadratic equation

Effect	Variable	Particle size		Entrapment efficiency	
		F- value	P- value	F- value	P- value
Linear effect	A	1529	< 0.0001	317.43	< 0.0001
	B	28.27	0.0011	32.80	< 0.0001
	C	76.49	< 0.0001	83.18	< 0.0007
Interaction effect	AB	106.24	< 0.0001	0.0000	-
	AC	19.95	0.0029	0.3599	-
	BC	2.95	-	0.8098	0.0300
Quadratic term	A ²	0.6573	-	0.0464	-
	B ²	95.34	< 0.0001	17.78	0.0040
	C ²	132.87	< 0.0001	23.35	< 0.0019

Table 3.4. Full quadratic model equations for particle size and entrapment efficiency generated by the design of expert software

CQA s	Coded equations	Predicted R ²	Adjusted R ²
Particle size	+ 118.80 + 40.25A + 5.50 B – 9.00 C + 15.00 AB – 6.50 AC – 2.50 BC - 1.15 A ² +13.85 B ² + 16.35 C ²	0.9569	0.9920
Entrapment efficiency (%)	+74.60 +10.50 A + 3.38 B +5.38 C + 0.0 AB + 0.5000 AC - 0.7500 BC - 0.1750 A ² -3.43 B ² -3.92 C ²	0.9106	0.9670

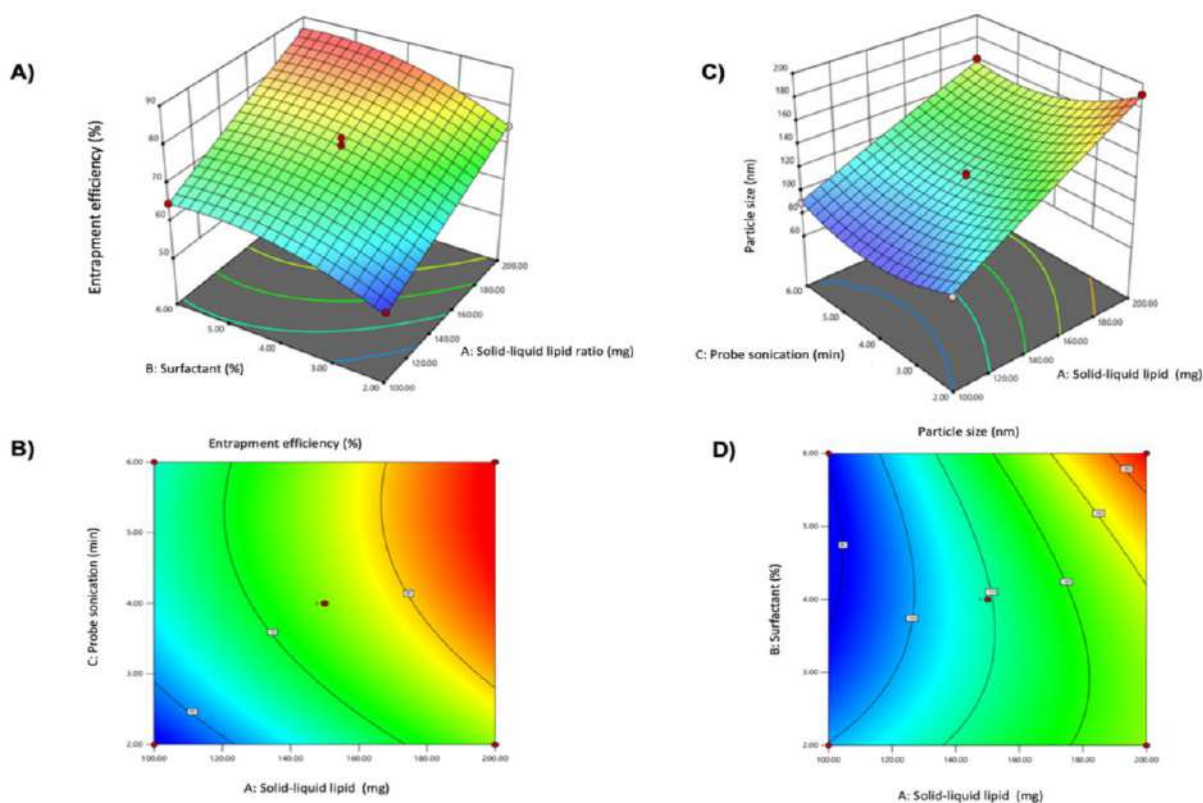


Figure 3.1. Box-Behnken optimization of surface response plots showing the effect of input variables particle size (nm) and entrapment efficiency (%) of ITZ/Ce6@LNPs. The 3D plot of input variables affecting response factor entrapment efficiency (%)A); The contour plot of input variables affecting response factor entrapment efficiency (%)B); The 3D plot of input variables affecting response factor particle size (nm) C); The contour plot of input variables affecting response factor particle size (nm) D).

The adjusted R^2 values (0.9920) and predicted R^2 values (0.9569) for particle size showed close agreement (with a difference of less than 0.2), while for entrapment efficiency, there was close agreement between the adjusted R^2 values (0.9670) and predicted R^2 values (0.9106) (with a difference of less than 0.2). The batch with a lipid amount of 180 mg, a surfactant concentration of 4 %, and a probe sonication time of 4 min was selected based on the experimental results. The predicted results for particle size and entrapment efficiency were validated by comparing them with the experimental results, and the % relative deviation was calculated and reported in **Table 3.5**. Increasing the amount of lipid while decreasing the concentration of surfactant and sonication time led to an increase in particle size. This is because as the lipid concentration increases, the viscosity of the melted lipid phase also increases, leading to a larger dispersion. On the other hand, a longer probe sonication time had a negative effect on particle size but a positive effect on entrapment efficiency. Similarly, surfactant concentration had a negative effect on particle size but a positive effect on entrapment efficiency. The optimal batch was

determined using a numerical method and desirability validation based on minimum particle size and maximum entrapment efficiency [23].

Table 3.5. Validation batch by the numerical method

Responses	Predicted results	Actual results	% Relative
Particle size (nm)	91.54 \pm 3.14	93.6860 \pm 4.7221	-6.32
Entrapment efficiency (%)	78.99 \pm 3.5	75.563 \pm 5.538	-26.44

In this formulation, we have used Precirol ATO and Squalene, which have been studied extensively for their potential as a component of lipidic nanoparticles in topical therapy. It has been shown to improve the stability and release of active ingredients from LNPs, as well as enhance their skin penetration ability. Herein the DOTAP (1,2-di-O-octadecenyl-3-trimethylammonium-propane), was the main component to maintaining the positive charge and stability of LNPs. Positively charged lipids are often used in LNPs because they can help to stabilize the lipid bilayer. The positively charged head group of DOTAP interacts with the negatively charged phosphate groups of other lipids in the bilayer, forming electrostatic interactions that can help to prevent the lipids from separating or aggregating. In addition to stabilizing the lipid bilayer, positively charged lipids like DOTAP can also improve the interaction of LNPs with target cells. The positively charged lipids can bind to negatively charged cell membranes, facilitating the uptake of the LNPs into the cell [24,25]. Additionally, We have used two surfactants such as Span 80 and Tween 20. The reason behind the selecting surfactants was the Hydrophilic lipophilic balance. In the formulation of lipidic nanoparticles, HLB values are used to select appropriate surfactants that can stabilize the nanoparticles and prevent them from aggregating or coalescing. This stabilizes the nanoparticles by creating a barrier between the hydrophobic core and the surrounding aqueous medium, preventing aggregation, coalescence, or precipitation [26] In addition to stabilizing the nanoparticles, surfactants with appropriate HLB values can also help to improve the drug loading and release properties of the formulation. By optimizing the HLB value of the surfactant or emulsifier, it is possible to achieve a better balance between hydrophilic and lipophilic interactions, which can enhance drug solubility and promote drug incorporation into the nanoparticle core. Overall, the HLB value plays a critical role in the stabilization of lipidic nanoparticle formulations by influencing the adsorption and orientation of surfactant or emulsifier molecules at the particle

interface. Therefore combining the two HLB value provides better stability and high drug loading [27,28].

3.3.1. Preparation of a combined Batch of ITZ and Ce6 (ITZ/Ce6@LNPs) and its characterization

After the finalization of the validated batch, the formulation batch was prepared for the dual drug-loaded lipid nanoparticle of ITZ and Ce6 by using low temperature followed by the probe sonication method. **Figure 3.2 A** represents the Formulation containing ITZ/Ce6@LNPs formulation (A-a); ITZ/Ce6@LNPs gel (SEPINEO™ P 600) (A-b). The prepared ITZ/Ce6@LNPs formulation was characterized using particle size, zeta potential, scanning transmission electron microscopic (STEM), and scanning electron microscope (SEM). The particle size, PDI, and zeta potential of the ITZ/Ce6@LNPs were determined by DLS and were found to be 92.98 ± 5.21 nm, 0.201 ± 0.021 , $+ 21 \pm 5.2$, respectively. The particle size and potential zeta graphs of ITZ/Ce6@LNPs are represented in **Figures 3.2 B & 3.2 C**. % drug loading and entrapment efficiency of ITZ was 4.11 % and 76.23 % and for Ce6 4.23 % and 79.2%. The respective SEM image of drug ITZ/Ce6@LNPs represented that the ITZ/Ce6@LNPs were uniformly fabricated, spherical shapes with a uniform particle size distribution, as shown in **Figure 3.2 D**. The UV spectrum overlay graph **Figure 3.2 E** represents the ITZ, Ce6, and ITZ/Ce6@LNPs formulations. ITZ shows a peak at 271 nm, while Ce6 shows two peaks at 400 nm and 666 nm. Similar peaks were observed for ITZ/Ce6@LNPs formulations when dissolved in ethanol. Therefore, it confirmed that the drugs were encapsulated into the ITZ/Ce6@LNPs, and the addition of ethanol disintegrated the ITZ/Ce6@LNPs. Periodical evaluation of particle size and the tracking of Ce6 and ITZ absorbance intensity over time for the LNPs stability on storage (**Figure 3.2 F**). The particle size was between 88.21 to 112 nm for ITZ/Ce6@LNPs on storage at 4°C for 24 days. Thus, the kinetic stability data revealed that insignificant deviation in the Ce6 signal in ITZ/Ce6@LNPs at 4 °C from day 1 to day 24.

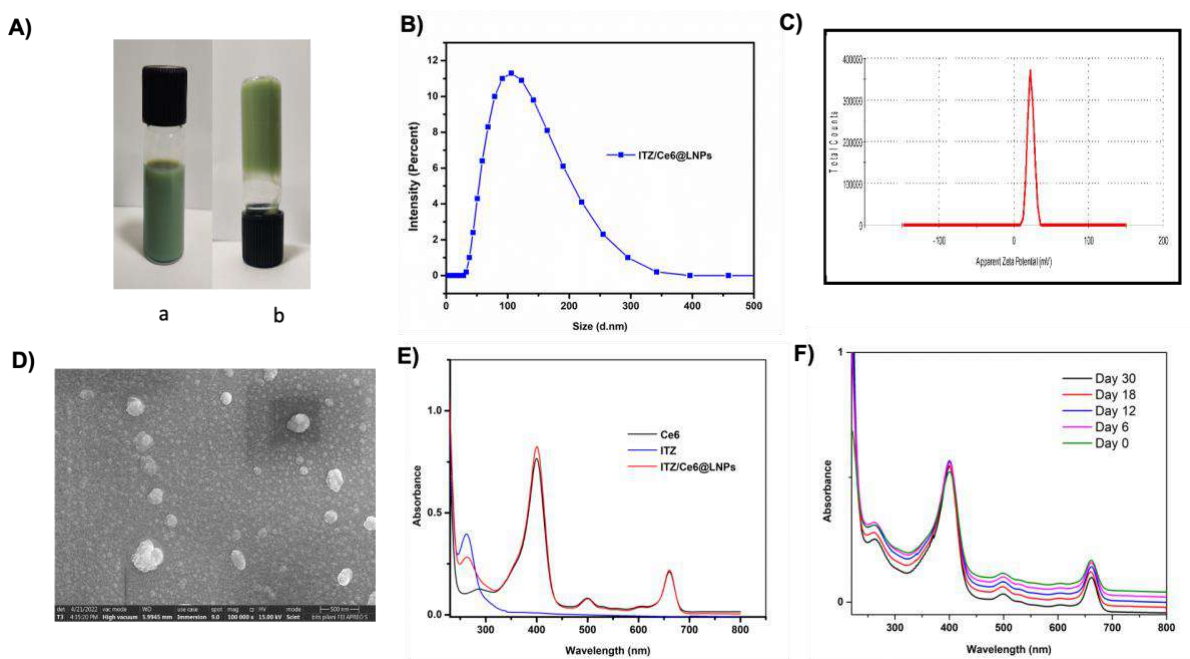


Figure 3.2. Physiochemical characterization of ITZ/Ce6@LNPs. Formulation containing ITZ/Ce6@LNPs formulation (A-a); ITZ/Ce6@LNPs gel (SEPINEO™ P 600) (A-b); Particles size distribution of ITZ/Ce6@LNPs (B); zeta potential of ITZ/Ce6@LNPs (C); Scanning electron micrograph of ITZ/Ce6@LNPs (D); UV absorbance spectra of free ITZ, free Ce6, and ITZ/Ce6@LNPs in methanol, (E); and Kinetic stability of ITZ/Ce6@LNPs (F).

3.3.2. Evaluation of the photoactivity and singlet oxygen generation

Fluorescence spectrophotometry was used to identify the photoactivity of ITZ/Ce6@LNPs and the generation of singlet oxygen ($^1\text{O}_2$) from ITZ/Ce6@LNPs following irradiation, as shown in **(Figure 3.3)**. Ce6 has maximum absorption at 405 and 640 nm. The free Ce6 or ITZ/Ce6@LNPs produced single oxygen with varied fluorescence intensity of DMA with 255000 and 89500, respectively. The reduction in fluorescence intensity of DMA has shown an increase in singlet oxygen generation. The ITZ/Ce6@LNPs generated higher than the free Ce6, as shown in **Figure 3.3 A**. Since free Ce6 was aggregated in the water, there was a decline in singlet oxygen generation **(Figure 3.3 B)**. However, there was a noticeable difference between the $^1\text{O}_2$ generation dissolved in ITZ/Ce6@LNPs and free Ce6 in DMSO.

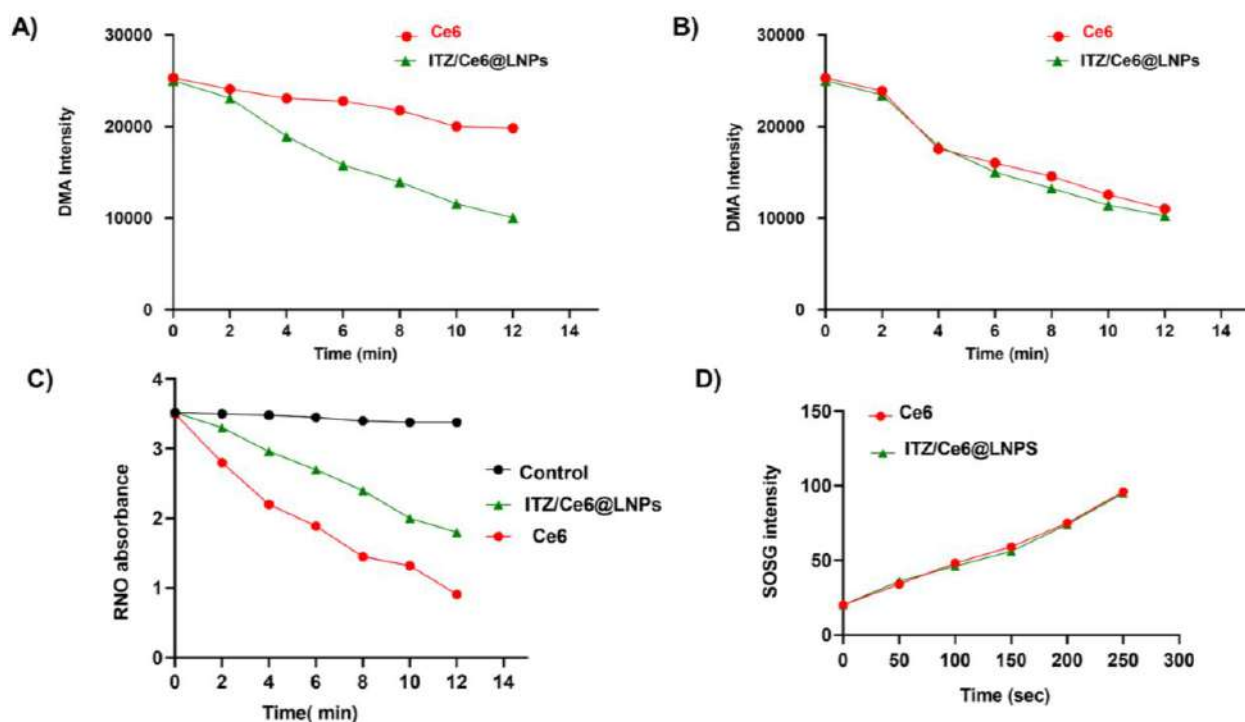


Figure 3.3 Biochemical analysis of Ce6-mediated ROS generation. Change in the fluorescence intensity of DMA (Ex. 360 nm; Em. 436 nm) w.r.t. time in the presence of free Ce6, ITZ/Ce6@LNPs in PBS (A), and in DMSO (B); time-dependent photo-bleaching of RNO by free Ce6, ITZ/Ce6@LNPs in PBS (C); Changes in fluorescence intensity of SOSG in the presence of free Ce6, ITZ/Ce6@LNPs in water (D).

Next, $^1\text{O}_2$ generation was investigated using RNO when histidine was present. The reaction was with histidine and RNO, the $^1\text{O}_2$ that was generated proceeds through a bleaching process. A transannular peroxide intermediate is formed when $^1\text{O}_2$ is taken in by the imidazole ring of the histidine molecule. The photobleaching occurs as a result of further interaction with RNO. The rate of formation of singlet oxygen was found to be determined by the variance in the photobleaching. Using a laser source with a wavelength of 660 nm, the ITZ/Ce6@LNPs, free ITZ, and free Ce6 were subjected to irradiation at a laser intensity of 0.5 W/cm^2 over different time durations. The absorbance of RNO was determined at 440 nm (**Figure 3.3 C**). When the irradiation time increased, the free Ce6 generated singlet oxygen at a faster rate than ITZ/Ce6@LNPs. This was proven by the substantial reduction in RNO absorbance. Due to the presence of a hydrophobic core in the nanocarrier, the entrance of histidine was limited, which led to the barrier in the formation of a singlet oxygen–histidine–RNO chain. Therefore leading to an unsuccessful detection of $^1\text{O}_2$.

The $^1\text{O}_2$ production capacity of DDLN in an aqueous solution was assessed using SOSG by evaluating the fluorescence and laser irradiation. The $^1\text{O}_2$ yield ITZ/Ce6@LNPs was significantly higher than free Ce6 (**Figure 3.3 D**).

3.3.3. In-vitro drug release

The drug release graph of developed ITZ/Ce6@LNPs and free drug of ITZ and Ce6 was represented in (**Figure 3.4**). Both free drugs showed 100% cumulative drug release within 6 h, while ITZ/Ce6@LNPs containing ITZ and Ce6 showed less than 50% cumulative release in 6 h and then 50 to 95% by the end of 24 h. The kinetic release model was investigated using a DD solver (add on Xcel sheet). The model of the release kinetics is shown in (**Table 3.6**), and it contains the correlation coefficient data, along with the AIC value and the MSC value. Throughout the process of evaluating the several models, the "best-fit" model was chosen to be the one that had the highest R^2 value, the lowest AIC, and MSC values which were higher than 2. It was confirmed by the tabulated data that the ITZ/Ce6@LNPs followed the 1st order kinetic model for both drugs (**Table 3.6**).

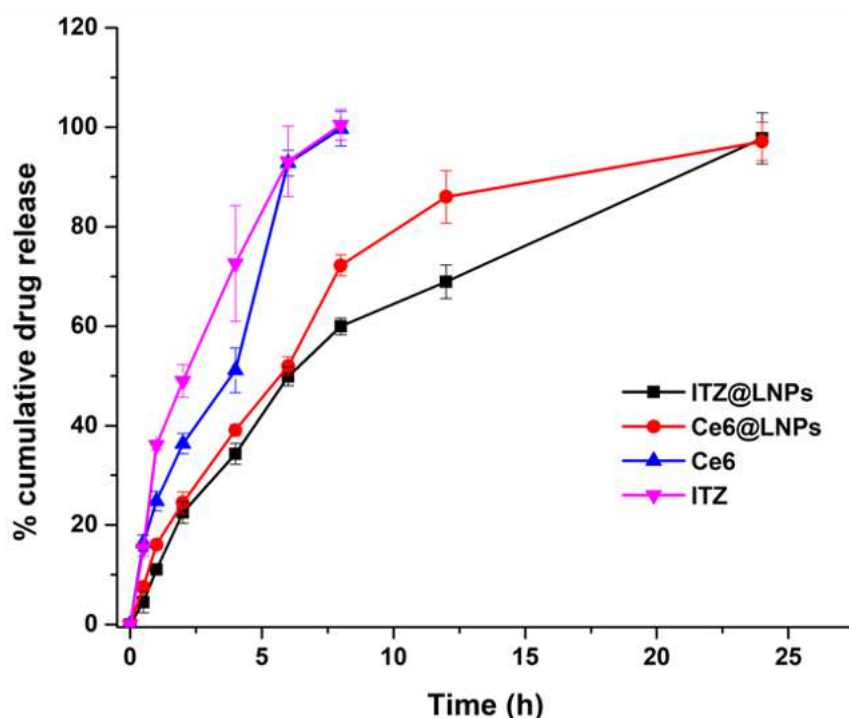


Figure 3.4 Represent the cumulative drug release graph of developed ITZ/Ce6@LNPs and free drug of ITZ and Ce6

Table 3.6. The release mechanism of ITZ/Ce6@LNPs formulation and free drugs by curve fitting method.

Kinetic models	Ce6 LNP				Free drug Ce6			
	R ²	k	AIC	MSC	R ²	k	AIC	MSC
Zero order	0.6611	5.3227	75.0595	0.6438	0.9399	13.7304	45.7677	2.2456
First order	0.9908	0.1419	42.6470	4.2452	0.9362	0.2719	46.1786	2.1869
Higuchi	0.9527	21.5567	57.3292	2.6138	0.9281	32.5342	47.0158	2.0673
Hixson Crowell	0.9901	0.0403	40.2222	4.5146	0.9548	0.0748	43.7621	2.5321
Koresmeyer peppas	0.9532 n =0.516	20.7454	59.2345	2.4021	0.9734 n=0.735	22.2110	42.0666	2.7743
Kinetic models	ITZ LNP				Free drug ITZ			
	R ²	k	AIC	MSC	R ²	k	AIC	MSC
Zero order	0.7971	4.9312	69.2784	1.1831	0.8393	14.8037	52.7657	1.1680
First order	0.9934	0.1112	38.5094	4.6019	0.9875	0.3717	34.8704	3.7244
Higuchi	0.9724	19.5520	51.3129	3.1792	0.9848	35.9905	36.2728	3.5241
Hixson Crowell	0.9895	0.0315	42.6155	4.1456	0.9867	0.0998	35.3436	3.6568
Koresmeyer peppas	0.9835 n =0.580	16.0485	48.6762	3.4722	0.9891 n= 0.557	32.8692	35.9417	3.5714

3.3.4. Characteristic of ITZ/Ce6@LNPs gel

The prepared ITZ/Ce6@LNPs formulation (**Figure 3.2 A a,)** was incorporated into a topical gel (SEPINEO™ P 600) (**Figure 3.2 A-b**). When nanoparticles are incorporated into a gel, they may form separation into gel or aggregates quickly. Thus, to ensure the microstructure of DDLN gel, SEM analysis was performed (**Figure 3.5 A**). The ITZ/Ce6@LNPs gel was a topical hydrogel preparation that was intended to be applied directly to the skin, and a pH analysis was required to confirm that the formulation remained unchanged. It was observed that the pH of the ITZ/Ce6@LNPs gel was 6.2 ± 0.7 , and this result was confirmed to be within the acceptable range for human skin pH (4.5–6.4). As a result, the optimized composition was identified as suitable for usage in order to reduce the risk of causing skin irritation during the application.

3.3.4.1. Rheological behaviour

The viscosity (η) of ITZ/Ce6@LNPs gel was found to be 70231 cP at 25 °C under the constant shear rate of 10 s⁻¹ (**Figure 3.5 B**). According to **Figure 3.5 B**, the rheograms exhibited non-Newtonian flow behaviour with shear-thinning characteristics and variable thixotropic behaviour. The thermal behaviour of the gel was determined by using temperature-dependent viscosity. In the temperature-dependent viscosity, by applying the constant share rate with varying temperatures from 25 to 40 °C viscosity was measured. As a result, it was confirmed that there were no changes in viscosity (**Figure 3.5 C**). To analyze the deformation behaviour and time-dependent behaviour of the sample, an amplitude sweep test and frequency sweep test were carried out. LVE demonstrates the extent to which analysis could be carried out without affecting the gel structure. In the amplitude sweep test, LVE region was found to be for ITZ/Ce6@LNPs 0.02 (% in terms of strain). **Figure 3.5 D** result demonstrates that G' is greater than G'', which indicates a solid viscoelastic structure or a gel-like structure. After identifying the LVE region, the frequency sweep test was performed to evaluate the gel stability during long-term storage as well as the flow behavior and internal structure of the ITZ/Ce6@LNPs gel. The obtained G' and G'' for ITZ/Ce6@LNPs gel were confirmed to be in the LVE region, and as a result (**Figure 3.5 E**), the sample has not changed over the course of the test.

3.3.4.2. Texture analyzer

To find out the texture of the gel, various parameters, including firmness, consistency, and cohesiveness, were recorded to obtain an interpretation of a gel texture. The firmness, consistency, and cohesiveness of ITZ/Ce6@LNPs gel were found to be 81.12 ± 5.12 g, 986 ± 23.12 g s⁻¹, and -452.65 ± 42 g, respectively (**Figure 3.5 F**). The above values indicated that the physical appearance of the gel was uniform and smooth, free from grittiness and or particulate matter. The results demonstrate that the DDLN gel could provide superior exclusiveness and also high effectiveness of loaded drugs in terms of the high permeability and retention of drugs in the application site.

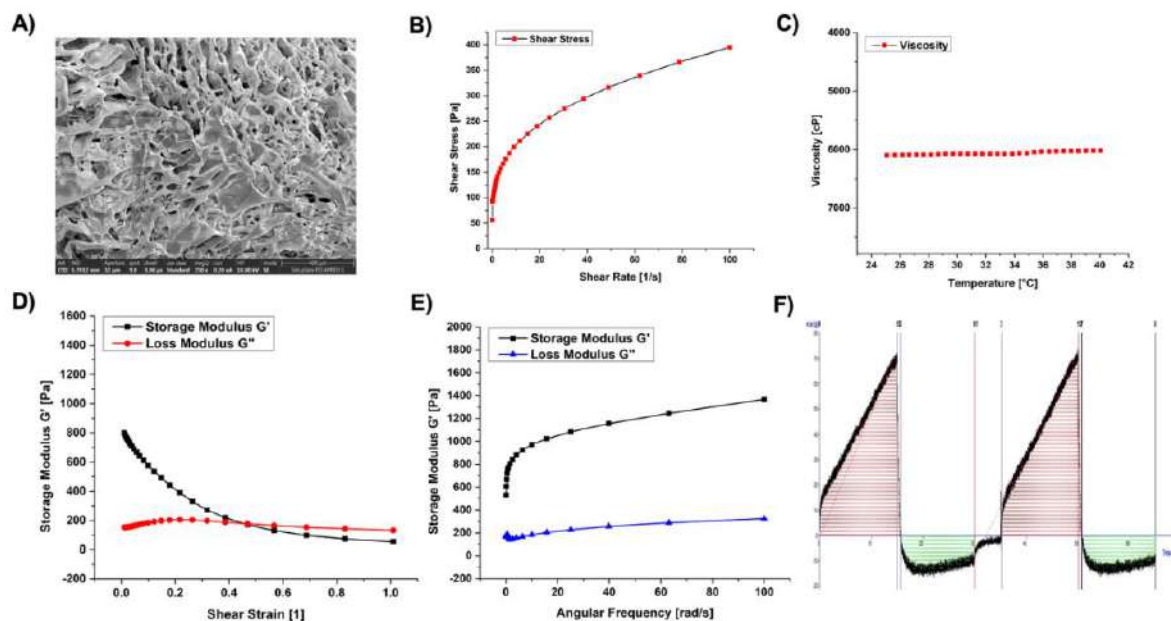


Figure 3.5 Characterization of ITZ/Ce6@LNPs gel; Scanning electron microscopic images of ITZ/Ce6@LNPs gel (A); Rheological behavior share stress vs share rate (B); temperature-dependent viscosity (25°C to 40 °C) (C); Amplitude sweeps test (D); Frequency sweep test (E); Texture analysis of ITZ/Ce6@LNPs gel (F).

3.3.4.3. Assessment of stability of ITZ/Ce6@LNPs and ITZ/Ce6@LNPs gel

The developed ITZ/Ce6@LNPs and ITZ/Ce6@LNPs gel were tested for storage stability for up to 90 days at two different temperatures such as 4 °C and 25 °C (**Table 3.7**). After being stored for a period of 90 days, the level of ITZ and Ce6 and did not significantly alter. Also, the results from the assay of the gel, particle size, and entrapment efficiency have not shown a substantial difference between 4 °C and 25 °C. It reveals that the ITZ/Ce6@LNPs and ITZ/Ce6@LNPs gel were stable with consideration of both the rheological and physiological characteristics.

Table 3.7 Stability data of ITZ/Ce6@LNPs and ITZ/Ce6@LNPs gel at different storage conditions

Stability condition	Days	ITZ/Ce6@LNPs	Particle size (nm)	% Entrapment efficiency (mean \pm SD)	Assay of nanocarrier loaded gel/ ITZ/Ce6@LNPs gel (mean \pm SD)
2-8 °C	0 day	Ce6	94.65 \pm 3.5	78.96 \pm 7.70	98.11 \pm 2.1
	0 day	ITZ		76.09.11 \pm .08	99.33 \pm 1.22
	30 days	Ce6	99.14 \pm 8.5	75.12 \pm 4.5	101.03 \pm 1.2
	30 days	ITZ		72.53 \pm 9.04	98.05 \pm 2.3
	90 days	Ce6	100.87 \pm 2.4	76.94 \pm 6.50	97.98 \pm 2.3

	90 days	ITZ		70.23 ± 5.43	99.09 ± 2.3
25 ± 0.5 °C	0 day	Ce6	90.4 ± 4.9	80.11 ± 6.32	98.22 ± 1.33
	0 day	ITZ		77.33 ± 4.33	99.12 ± 2.76
	30 days	Ce6	101.15 ± 10.2	76.12 ± 13.4	97.22 ± 4.10
	30 days	ITZ		75.12 ± 6.08	98.11 ± 1.3
	90 days	Ce6	112.56 ± 4.9	72.23 ± 12.3	97.11 ± 2.1
	90 days	ITZ		70.09 ± 17.12	99.11 ± 1.9

3.3.5. In-vitro assays

3.3.5.1. Cellular uptake

The cellular internalization of Ce6 and ITZ/Ce6@LNPs was evaluated using fluorescence microscope and flow cytometry techniques. This allowed for both qualitative and quantitative analysis of the internalization process in B16F10 and A431 cells. In both cell lines, a distinct and intense red fluorescence was observed in the cytoplasm and nuclei of cells treated with ITZ/Ce6@LNPs, indicating rapid internalization of the ITZ/Ce6@LNPs. The red fluorescence intensity of Ce6 and ITZ/Ce6@LNPs increased from 1 to 4 h, indicating a time-dependent cellular uptake in both B16F10 and A431 cell lines (**Figure 3.6A** for B16F10 cells and **Figure 3.6 B** for A431 cells).

Furthermore, flow cytometry studies were conducted to validate the enhanced internalization and intracellular release of ITZ/Ce6@LNPs. The histogram analysis of mean fluorescence intensity demonstrated an increase in values for ITZ/Ce6@LNPs and Ce6 from 1 to 4 h. These results were visually represented as bar graphs (**Figure 3.7A** for B16F10 cell lines and **Figure 3.7B** for A431 cell lines) to illustrate the observed changes in fluorescence intensity over time. The geometric mean fluorescence of ITZ/Ce6@LNPs (+ L) treated cells from 1522.2 ± 12.22 to 3343.54 ± 16.27 from 1 to 4 h for B16F10 cells, whereas the geometric mean fluorescence of free Ce6-treated cells was increased from 746.4 ± 33.7 to 1603.7 ± 23.67 . Similarly, the geometric mean fluorescence of ITZ/Ce6@LNPs (+ L) treated cells from 1712.32 ± 10.32 to 3890.54 ± 22.27 from 1 to 4 h for A431 cell lines. (**Figure. 3.7 C** for B16F10 and **Figure 3.7 D** for A431 cell lines). The time-dependent increase in fluorescence could be easily observed in both cell lines by the shift in the peak.

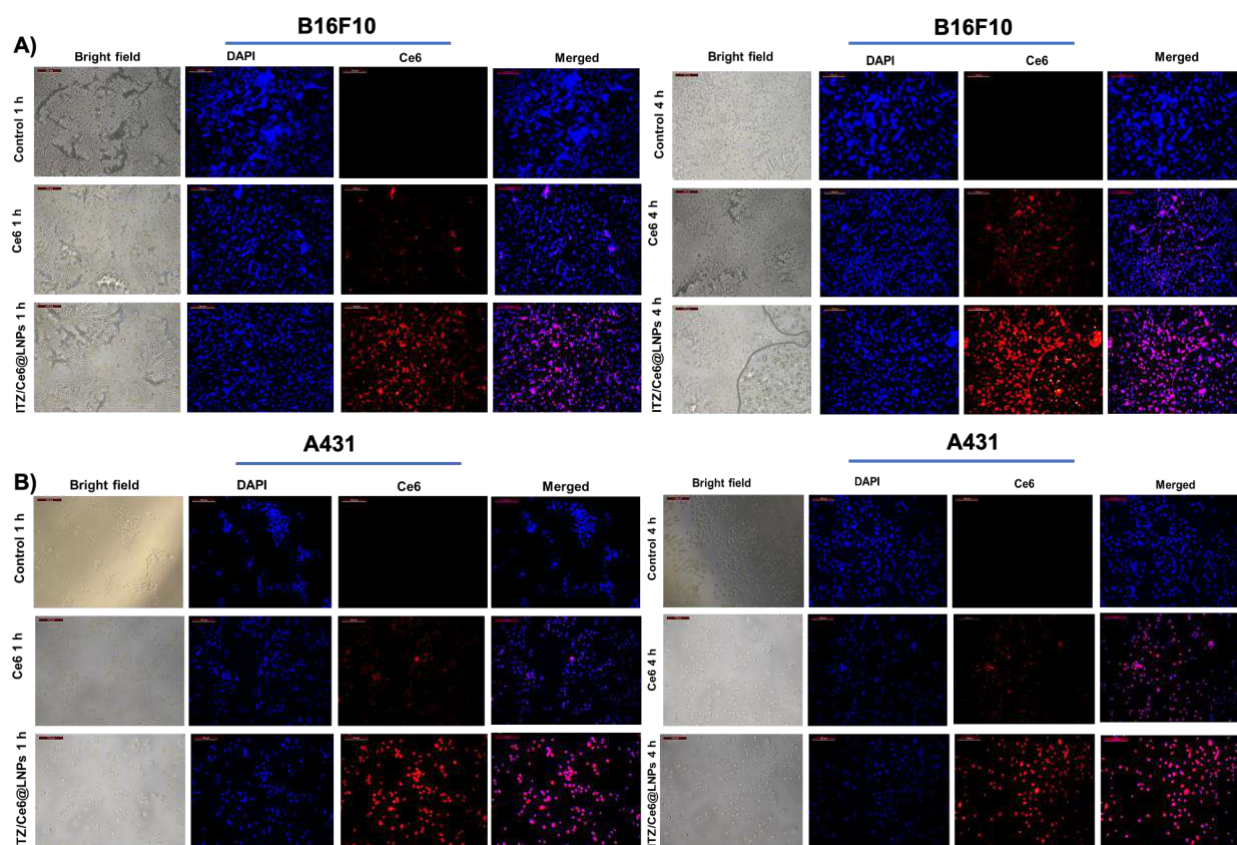


Figure 3.6. Cellular uptake study of free ce6, ITZ/Ce6@LNPs in B16F10 (A) and A431 cell lines (B) cells after 1 and 4 h of incubation (Ce6 concentrations. 6 μ g/ml). Red and blue, and signals represent cells stained by Ce6 and DAPI, respectively.

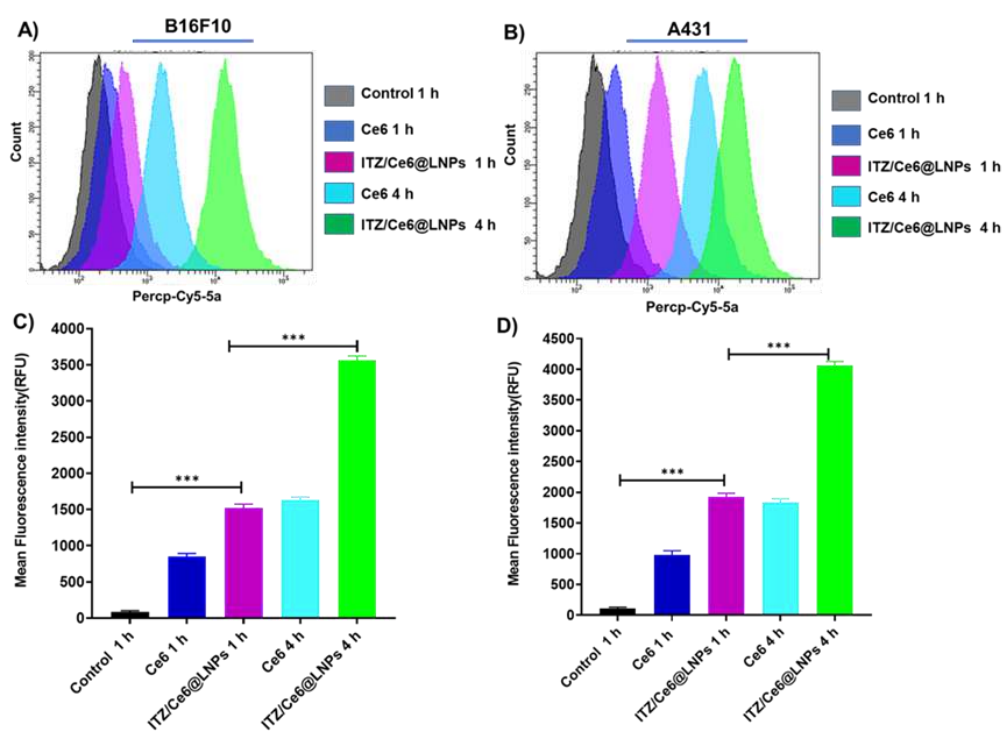


Figure 3.7. The histogram and bar graph represent the quantitative uptake of NPs using flow cytometry for B16F10 (A) and (C), respectively; Assessment of the geometric mean of fluorescence of the A431 at 1 and 4 h incubation by histogram plots and bar graphs (B) and (D). The data in bar graphs represent mean \pm standard deviation, calculated from three sets of experiments (**p < 0.01).

3.3.5.2. Cell viability assay

The MTT assay indicated a time and concentration-dependent decrease in the cell viability in both B16F10 and A431 cell lines for the various formulations treated, as represented in **Figures 3.8 and 3.9**. The figure illustrates that the positive control group (+L alone) exhibited similar cell survival rates compared to the negative control group (PBS, -L), indicating that laser irradiation alone did not cause significant harm to the cells. In general, the cells subjected to laser irradiation (+L) displayed higher levels of cell death compared to the non-irradiated cells (-L) at both 24 and 48 h. As the intensity, dose, and duration of ITZ/Ce6@LNPs increased along with laser treatment, the number of surviving cells decreased, indicating a dosage, time, and laser-dependent relationship. The strong inhibitory effect of ITZ/Ce6@LNPs without laser could be attributed to the release of Ce6 and ITZ.

It was observed that the cytotoxic effect was highest for ITZ/Ce6@LNPs, followed by ITZ+Ce6 as compared to free Ce6 and ITZ. The ITZ/Ce6@LNPs showed an IC₅₀ of 11.12 μ g/ml for 24 h on B16F10 cell lines, which was lower than the IC₅₀ of free Ce6 (+ L), ITZ (+L), and ITZ+Ce6 (+L), which were 20.14 μ g/ml, 26.12 μ g/ml, and 14.12 μ g/ml, respectively. Similarly, ITZ/Ce6@LNPs (+ L) treatment for 24 h on A431 cell lines showed an IC₅₀ of 9.81 μ g/ml, while free Ce6 (+ L), free ITZ (+ L), and ITZ+Ce6 (+ L) exhibits IC₅₀s of 19.14 μ g/ml, 23.45 μ g/ml, and 12.41 μ g/ml, respectively. Interestingly, the ITZ/Ce6@LNPs treatment showed the lowest IC₅₀ values of any of the conditions that were assessed. The ~3.1 fold decrease in IC₅₀ values of ITZ/Ce6@LNPs than free Ce6 and free ITZ at 24 h (+L). Therefore, it indicates that the longer retention of ITZ/Ce6@LNPs intracellularly reaches optimum concentration to exert cytotoxic action.

3.3.5.3. Combination index analysis

Combination indexes (CI) at all tested fractions affected, including IC₁₀, IC₂₀, IC₃₀, IC₄₀, IC₅₀, IC₆₀, IC₇₀, IC₈₀, and IC₉₀ for both the cell lines and at all the tested treatment regimens (24 h + L, - L) and (48 h + L, -L) were represented in **Figure 3.8 E, F, G, and H and 3.9 E, F, G, and**

H. The lowest CI was observed at 24 h (+L), and 48 h (+L) time point at 50 % fraction affected as mentioned in **Table 3.8** for in B16F10 and A431 cell lines. It was observed that ITZ/Ce6@LNPs formulation with a drug loading ratio of 1:1 showed a synergistic effect for both cell lines, with combination indices values below 1.

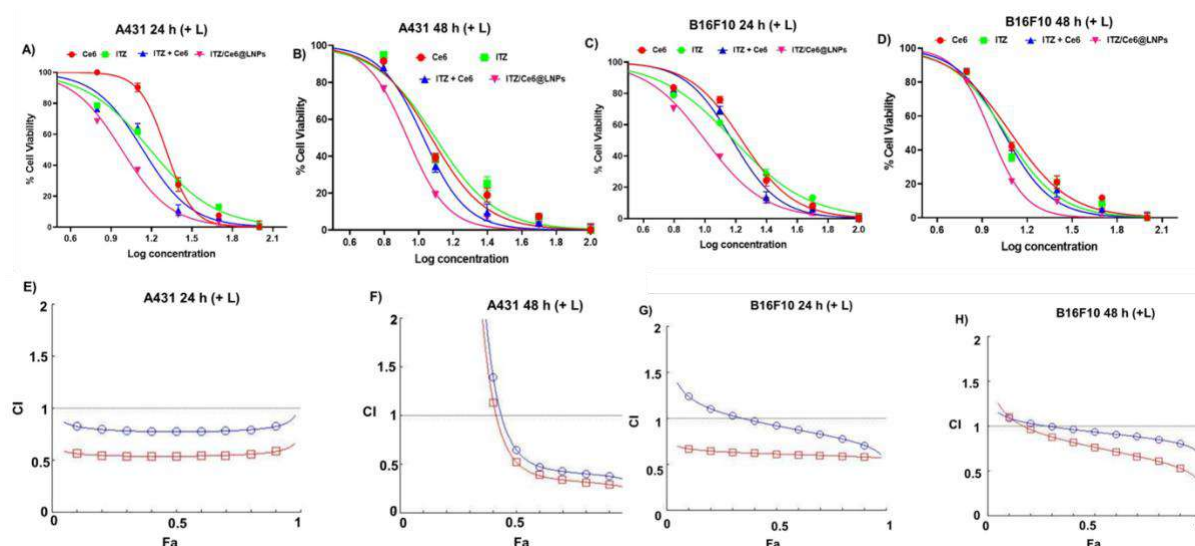


Figure 3.8. The dose-response curve for the determination of IC_{50} values of free ITZ, free Ce6, ITZ+Ce6, and ITZ/Ce6@LNPs (24 and 48 h) in cultured A431 (A and B) and B16F10 cell lines (C and D) with (+L) laser; graphs representing combination index (CI) in A431 (E and F) and B16F10 cells (G and H) with (+L) laser.

Table 3.8. The combination index value of ITZ/Ce6@LNPS

Group	CI value (B16F10 cell lines)	CI value (A431 cell lines)
IC_{10}	0.980	0.862
IC_{20}	0.934	0.832
IC_{30}	0.919	0.817
IC_{40}	0.900	0.801
IC_{50}	0.880	0.790
IC_{60}	0.864	0.760
IC_{70}	0.836	0.754
IC_{80}	0.828	0.738

IC ₉₀	0.781	0.726
------------------	-------	-------

3.3.5.4. Annexin V assay

In order to explore the relationship between cell growth suppression and cell cycle progression, flow cytometry was utilized to analyse the cell cycle distribution of B16F10 and A431 cells. The extent of apoptosis for free ITZ, free Ce6, ITZ+Ce6, and ITZ/Ce6@LNPs formulations is shown in **Figures 3.10 A and B**. It can be observed that for B16F10 cell lines, while free Ce6 (- L, +L) showed an apoptosis % of 10.23 %, and 13.40 %, free ITZ (- L, + L) showed apoptosis of 9.58 %, 9.72 %, ITZ+Ce6 (- L, + L) showed apoptosis of 18.32 %, 20.58 %, and ITZ/Ce6@LNPs (- L, + L) showed apoptosis of 35.58 %, 45.14 %. Similarly, in A431 cell lines, free Ce6 (- L, +L) showed an apoptosis % of 14.25 %, 17.25 %, free ITZ (- L, + L) showed apoptosis of 12.24 %, 16.04 %, ITZ+Ce6 (- L, + L) showed apoptosis of 24.2 %, 33.07 %, and ITZ/Ce6@LNPs (- L, + L) showed apoptosis of 40.41 %, 63.24 %.

The ITZ/Ce6@LNPs (+L) formulation exhibited the highest apoptotic response in both cell lines, suggesting that multiple factors contribute to this effect. These factors may include the high cellular uptake and retention of ITZ/Ce6@LNPs within cellular compartments, as well as the combined chemo-photodynamic therapy mediated by Ce6 and ITZ. The results further supported the previous findings on cytotoxicity, demonstrating that ITZ/Ce6@LNPs treatment (+L) was more effective in terms of therapeutic impact compared to free ITZ, Ce6, and ITZ+Ce6 treatments

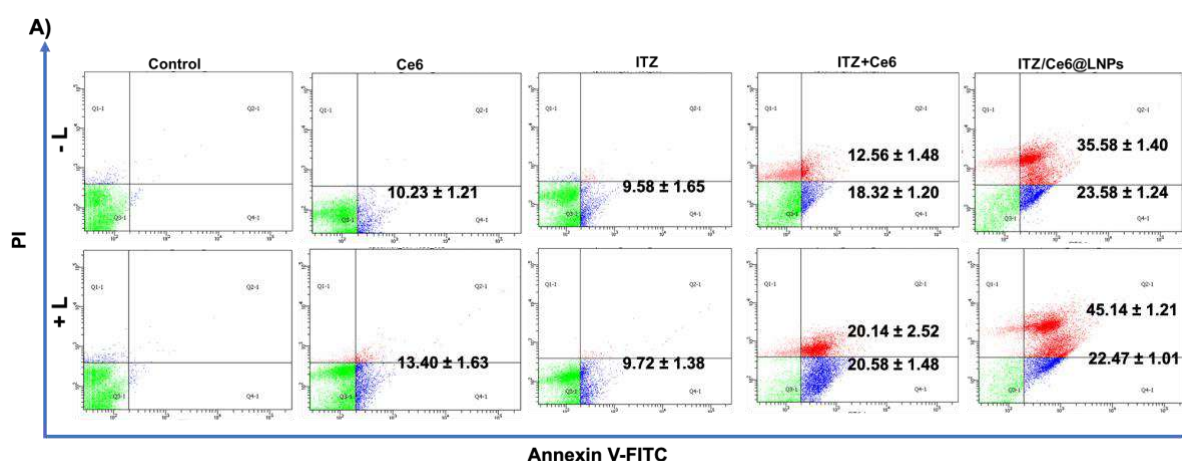
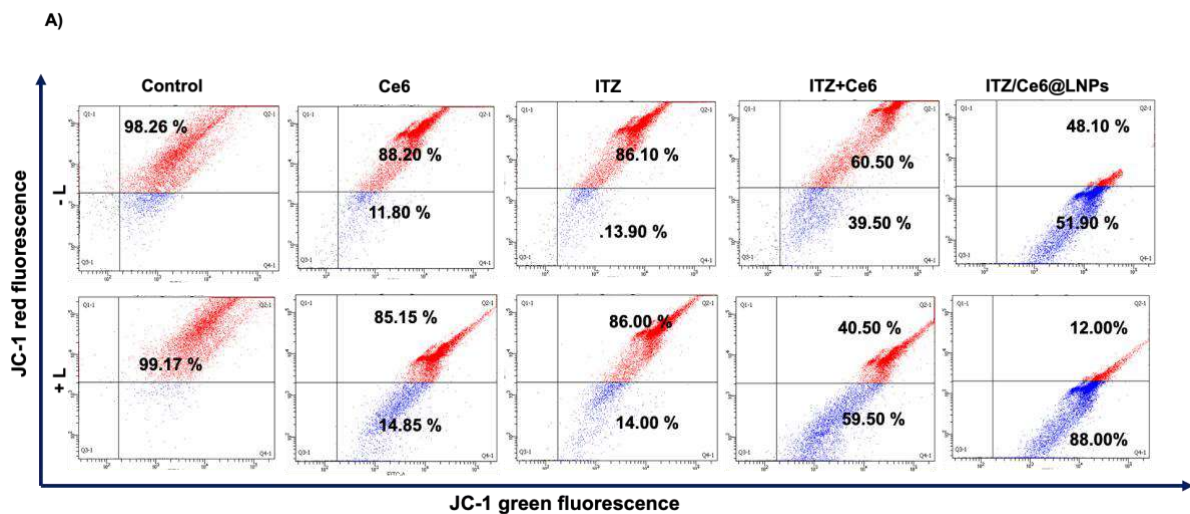


Figure 3.10. Annexin V assay performed by flow cytometry. The extent of apoptosis was evaluated by analyzing B16F10 cells (A) and A431 cells (B) treated with free ITZ, free Ce6, ITZ+Ce6, and ITZ/Ce6@LNPs (with and without laser, +L, -L) at a Ce6 and ITZ concentrations of 10 µg/ml (incubation time. 24 h) by using flow cytometry. Untreated cells are designated as control. The Q3

and Q4 quadrants represent early and late apoptosis, respectively (gated cell number. 10,000); the numerals represent the quantified percent cell populations in Q2 quadrants.

3.3.5.5. Mitochondrial membrane potential (MMP)

Mitochondrial membrane potential (MMP) refers to the difference in electrical potential across the inner mitochondrial membrane, which is maintained by the proton gradient generated during oxidative phosphorylation. It is a crucial parameter that reflects the functional state of mitochondria and has implications in cellular metabolism, signaling, and apoptosis. JC-1, a cationic dye, is utilized to assess MMP. In healthy mitochondria, JC-1 forms aggregates emitting red fluorescence, while in depolarized or dysfunctional mitochondria, it remains in a monomeric form, emitting green fluorescence. Mitochondrial damage can be exacerbated by the production of reactive oxygen species (ROS), leading to cellular apoptosis. To investigate the effect of free ITZ, Ce6, ITZ+Ce6, and ITZ/Ce6@LNPs treatment on MMP, we examined A431 and B16F10 cells. Flow cytometry analysis revealed that treatment with ITZ/Ce6@LNPs resulted in a greater disruption of MMP in both cell lines, as depicted in **Figures 3.12A and B** (B16F10) and **3.13A and B** (A431).



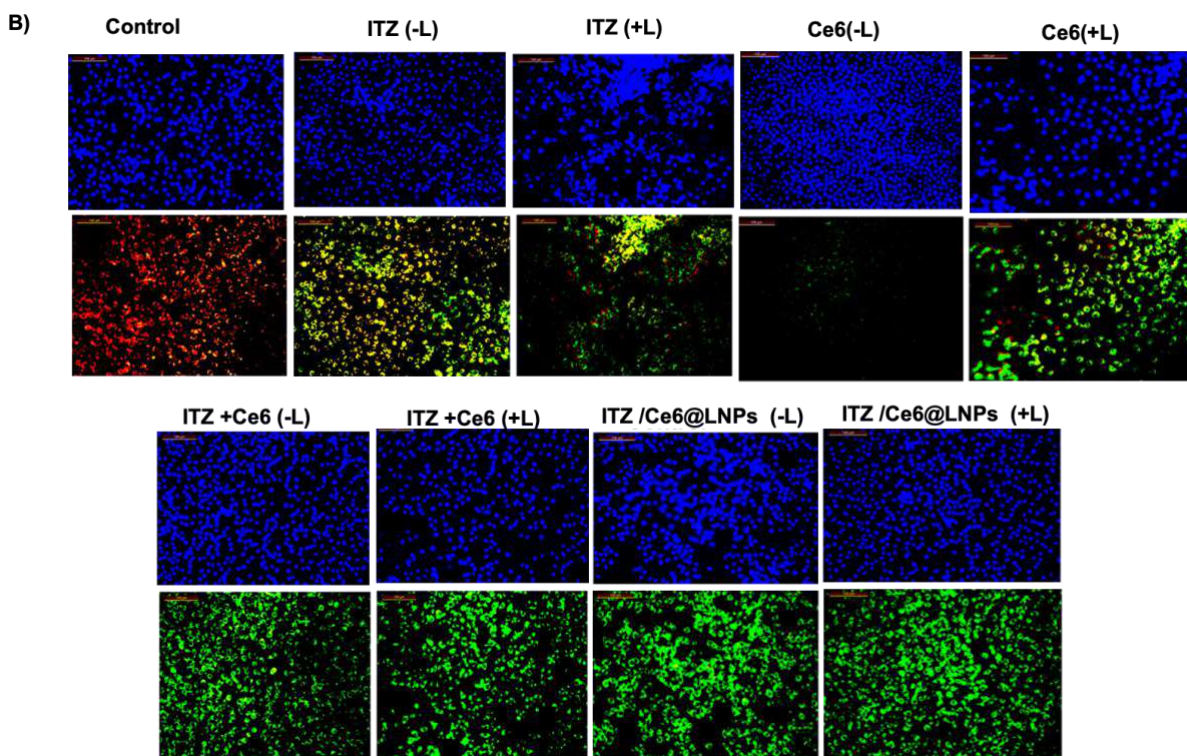


Figure 3.12. Qualitative and quantitative assessment of mitochondrial membrane potential in B16F10 cells treated with free Ce6, ITZ, ITZ+Ce6, ITZ/Ce6@LNPs followed by incubation of cells with mitochondria depolarization indicator JC-1 dye by flow cytometry (A) and fluorescence microscopy (B), and The JC-1 fluorescence was visualized under a laser, ex/em. 488/530 nm in both fluorescence microscopy and flow cytometry. Gated cell population. 10,000 for the flow cytometry analysis.

3.3.5.6. Reactive oxygen generation assay

To observe the formation of reactive oxygen species (ROS) induced by ITZ/Ce6@LNPs, the intracellular sensor DCFH-DA dye was utilized in both B16F10 and A431 cell lines. Remarkable green fluorescence was observed in B16F10 and A431 cells treated with ITZ, Ce6, ITZ+Ce6, and ITZ/Ce6@LNPs in the presence of laser irradiation. However, no significant green fluorescence was observed in the absence of laser irradiation. These observations suggest that the NPs induced higher intracellular ROS production when combined with laser irradiation. This phenomenon indicates the potential benefits of ITZ/Ce6@LNPs in enhancing the outcomes of chemo-photodynamic combination therapy and effectively killing cancer cells, as depicted in **Figure 3.15A** (B16F10) and **3.15 B** (A431).

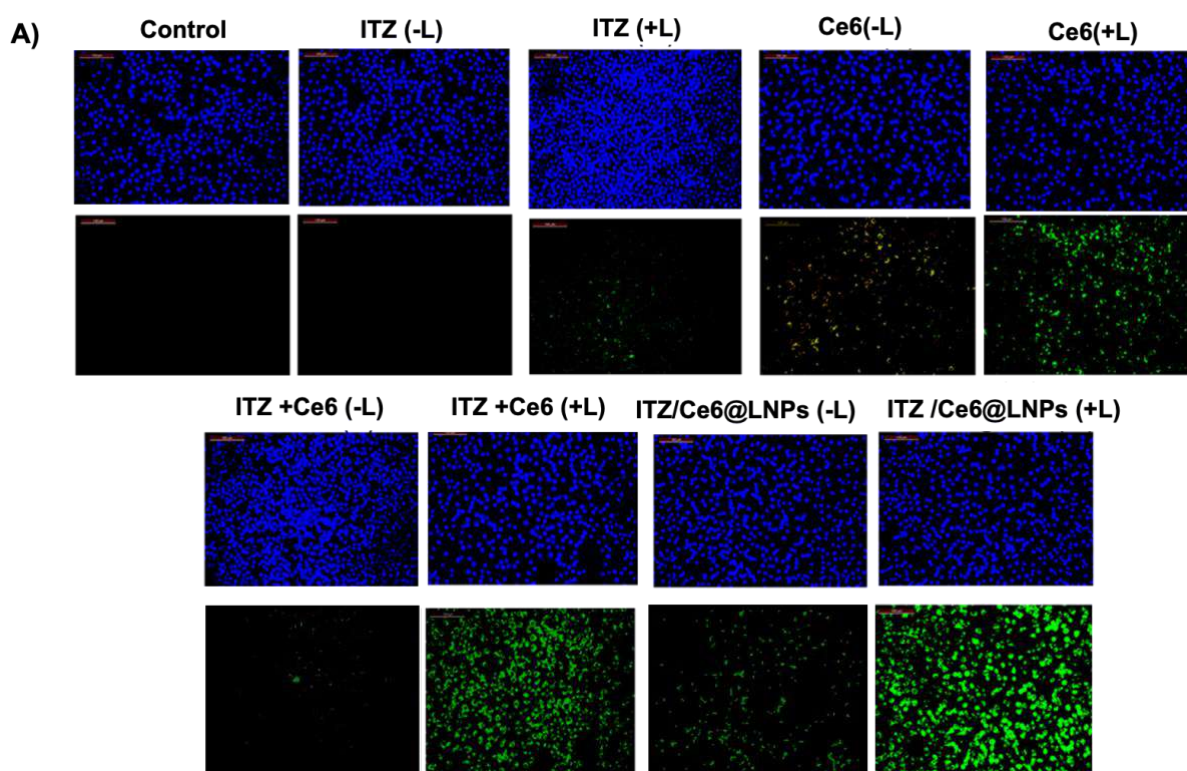


Figure 3.15: Intracellular ROS generation in B16F10 and A431 cells treated with free ITZ, free Ce6, ITZ+Ce6, and ITZ/Ce6@LNPs (with and without laser,+L,-L) by fluorescence microscopy (A) and (B) Untreated cells are designated as control. The ROS level was detected by tracking the fluorescence of DCFHDA dye (ex/em. 488/525 nm).

3.3.5.7. Nuclear staining assay

DAPI is a fluorescent stain that has a strong affinity for A-T-rich regions of DNA, making it useful for visualizing chromatin condensation or nuclear damage. It can differentiate between living cells and apoptotic cells by staining the condensed nuclei of apoptotic cells with a bright blue color. Therefore, we employed DAPI staining to detect apoptosis induction in A431 cells and B16F10 cells treated with ITZ, Ce6, ITZ+Ce6, and ITZ/Ce6@LNPs. **Figures 3.16 A and B** exhibit the nuclear fragmentation (NF) and cytoplasmic shrinkage (CS) observed in the cells with the various treatments. Blebbing was observed, which is considered a marker for apoptosis. It was observed that the cells treated with ITZ/Ce6@LNPs formulation showed the highest cellular damage highlighting the synergistic effect of Ce6 and ITZ. The AO-EtBr techniques were used in order to provide an understanding of the mechanism in which cells died, namely in terms of apoptosis and necrosis. The vital dye AO can stain every cell, whether they are alive or dead, while cells whose membrane integrity has been disrupted can take up

the stain EtBr. And hence, normal cells which remain intact appear to be green, whereas cells that are in the early or late stages of apoptosis and have compressed or damaged nuclei appear to be yellowish-orange or reddish, respectively. AO penetrated normal or early apoptotic cells, producing green fluorescence after binding with DNA. However, EB could only enter through damaged membranes and emitted orange-red fluorescence after binding to condensed apoptotic nuclei. In contrast, necrotic cells stain orange but possess normal nuclear morphology with no condensed chromatin. The assay could detect normal cells, cells at different stages of apoptosis, and necrotic cells by changing cellular fluorescence and morphology. Both B16F10 and A431 cell lines were undergoing apoptosis after ITZ/Ce6@LNPs treatment, as indicated by an orange fluorescence.

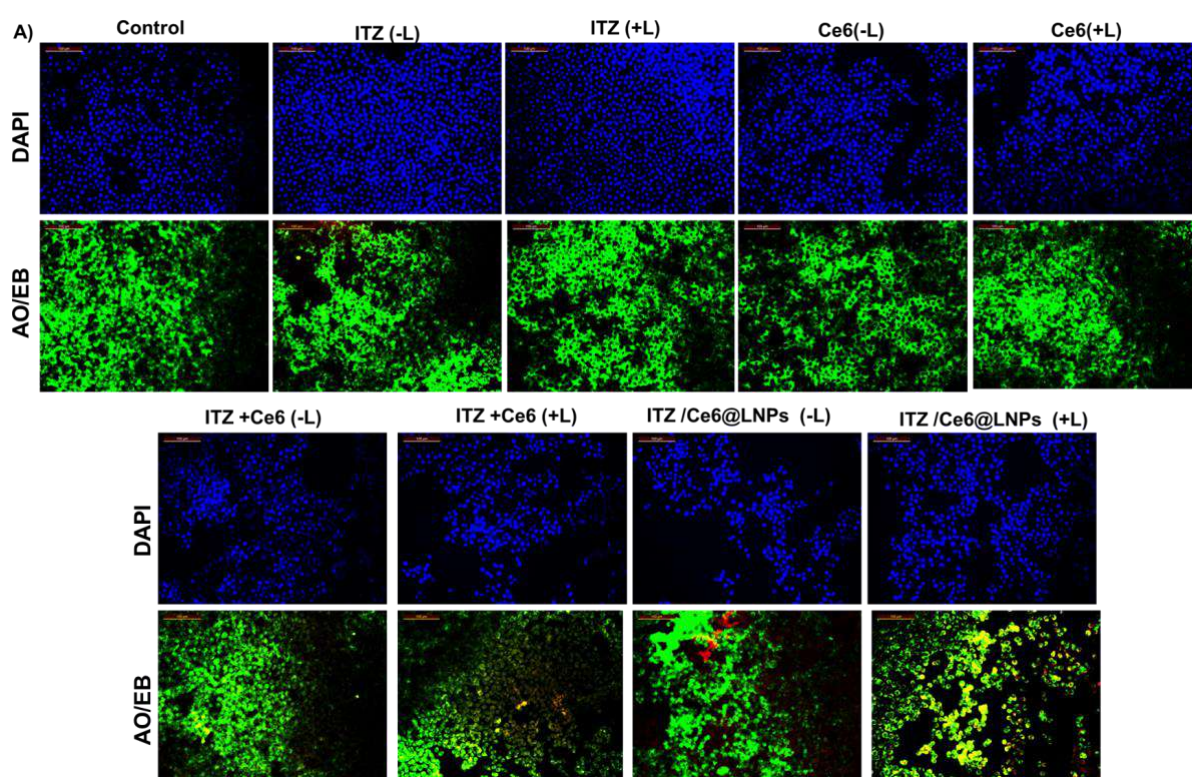


Figure 3.16. Analysis of nuclear morphology. Examples of B16F10 (A) and A431 cells (B) stained with DAPI, acridine Orange, and ethidium bromide following the treatment by free ITZ, free Ce6, ITZ+Ce6, and ITZ/Ce6@LNPs (ITZ and Ce6 concentration 10 $\mu\text{g/ml}$) (control cells received no treatment) (with and without laser, +L, -L), visualized under a fluorescence microscope on 40x Magnification. Scale bar. 50 μm .

3.3.6. Ex-vivo Studies

3.3.6.1. Ex-vivo Skin Permeation Study

The Franz diffusion cell, was utilized in the skin permeation study. **Figure 3.17 A** shows the *ex-vivo* permeation of ITZ/Ce6@LNPs and plain gel (ITZ+Ce6) formulation permeated

through goat skin. The amount of ITZ and Ce6 permeated (% permeation) through ITZ/Ce6@LNPs gel and plain gel (ITZ+Ce6) after 24 h was found to be up to 78 % and 30 %, respectively (**Figure 3.17 A**). The permeation ($\mu\text{g}/\text{cm}^2$) of ITZ and Ce6 drugs from ITZ/Ce6@LNPs gel and plain gel (ITZ+Ce6) through the goat skin was about upto 68 $\mu\text{g}/\text{cm}^2/24$ h and up to 30 $\mu\text{g}/\text{cm}^2/24$ h respectively (**Figure 3.17 B**), which indicates ITZ/Ce6@LNPs gel has significantly higher skin permeation than the plain (ITZ+Ce6). The flux value of ITZ/Ce6@LNPs gel containing ITZ and Ce6 was found to be 7.1303 ± 0.97 $\mu\text{g}/\text{cm}^2/\text{h}$, 6.296 ± 0.24 $\mu\text{g}/\text{cm}^2/\text{h}$ respectively. Additionally, the flux values of plain gel (ITZ+Ce6) containing ITZ and Ce6 were found to be 1.4166 ± 0.32 $\mu\text{g}/\text{cm}^2/\text{h}$, 1.1803 ± 0.21 $\mu\text{g}/\text{cm}^2/\text{h}$, respectively. The ITZ/Ce6@LNPs gel demonstrated more ability to penetrate the goat skin than the plane gel, which was attributable to the enhancement of penetration by the DOTAP lipid (cationic charge-based lipid), solid lipid, and liquid lipid. The positively charged head group of the cationic lipid can interact with the negatively charged head groups of the lipids in the stratum corneum. This interaction can disrupt the organized structure of the stratum corneum and create temporary pathways for the drug to penetrate the skin. Additionally, the positively charged head group of the cationic lipid can interact with the negatively charged cell membranes of the skin cells, which can facilitate the penetration of the drug into the skin. Furthermore, positive charge lipids can also form complexes with drugs, called cationic lipid-drug complexes. These complexes can improve the solubility and stability of drugs, allowing them to penetrate the skin more effectively. Additionally, Positive charge-based lipids (DOTAP) can form an interaction between extracellular lipid matrices of the skin resulting in the disruption of lipid orientation, which creates the diffusion or pathway to cross nanoparticles through the skin.

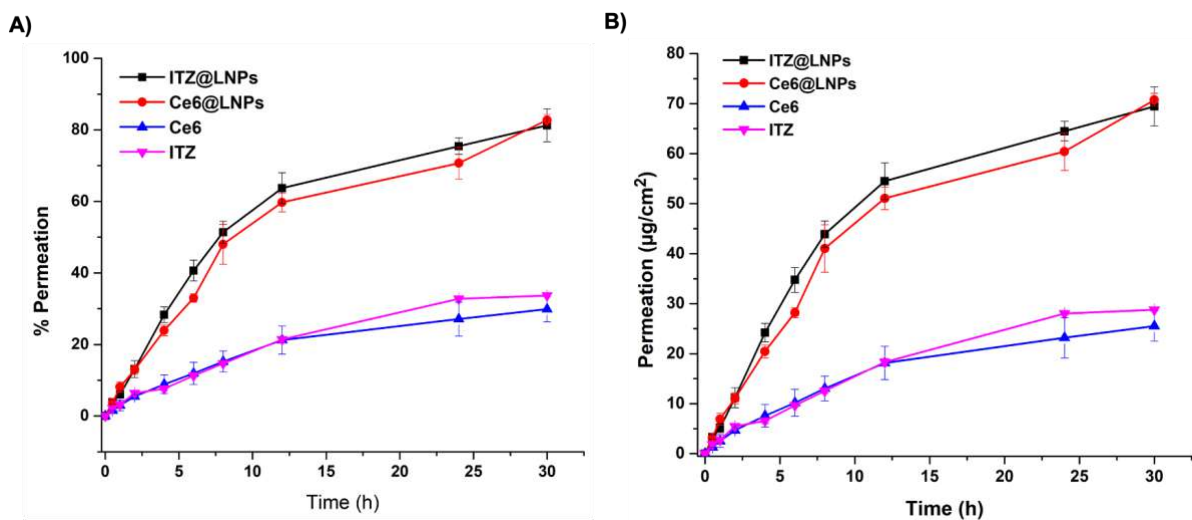


Figure 3.17. Ex vivo skin permeation profile of ITZ/Ce6@LNPs and free ITZ and free Ce6 permeated through the skin (% Permeation) (Data represented as mean \pm SD, n = 3) (A); Ex vivo skin permeation profile of ITZ/Ce6@LNPs and free ITZ and Ce6 permeated through the skin ($\mu\text{g}/\text{cm}^2$) (Data represented as mean \pm SD, n = 3) (B).

3.3.6.2. Ex vivo bioimaging in tumor skin of the C57/BL6 mice

In **Figure 3.18A** of the study, the bioimaging results of tape-stripped ex vivo skin cancer tissue are presented. The tissue was treated with either free ITZ+Ce6 gel or ITZ/Ce6@LNPs gel for 6, 12, and 24 h using Franz diffusion cells. Images were captured using the In Vivo Imaging System (IVIS PerkinElmer, Inc., USA) to excite Ce6 at 405 nm and record the corresponding emission at 665 nm. The results demonstrate that the ITZ/Ce6@LNPs gel exhibited significantly higher fluorescence compared to the free ITZ+Ce6 gel at all time points. This indicates that the incorporation of ITZ/Ce6 into LPNs enhanced the penetration of the drug into deeper layers of the skin.

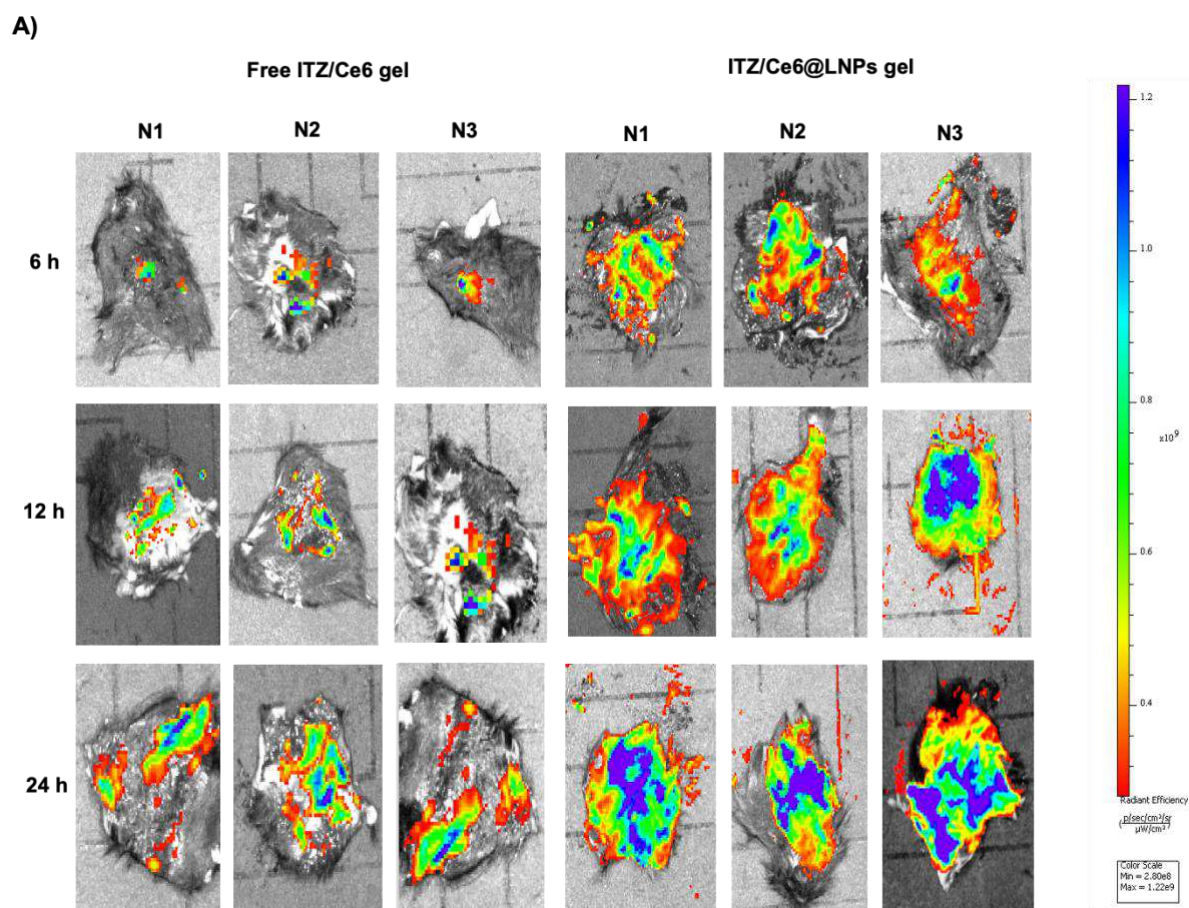


Figure 3.18. A Bio-imaging using IVIS spectrum of tape-stripped ex vivo skin cancer tissue treated with either free ITZ+Ce6 gel or ITZ/Ce6@LNPs gel at 6, 12, and 24 h (Data represented as mean \pm SD, n = 3).

3.3.6.3. Topical In Vivo Biodistribution Study in C57/BL6 Mice Skin Cancer Model

The biodistribution of free Ce6 and ITZ/Ce6@LNPs gel was investigated topically in B16F10 tumor-bearing mice to study there in vivo distribution. The fluorescence distribution of Ce6 was observed at various time points (0.5, 1, 3, 6, 12, 24, and 48 h) after topical application. The results showed that the fluorescence intensity at the tumor site of the ITZ/Ce6@LNPs gel-treated group gradually increased up to 12 h post-application. In contrast, the free Ce6-treated group exhibited a significantly lower signal, indicating that the ITZ/Ce6@LNPs gel may accumulate more effectively at the tumor site (**Figure 3.19A**). **Figure 3.19B** demonstrates the total body fluorescence intensity over time. It can be observed that even 48 h after topical application, the tumor in the ITZ/Ce6@LNPs gel-treated group still exhibited a strong fluorescence signal, indicating the high targeting and retention capacity of the ITZ/Ce6@LNPs gel. The mice were topically treated with ITZ/Ce6@LNPs gel, and after 48 h, they were

sacrificed, and their major organs and tumor tissues were collected for fluorescence imaging, as depicted in **Figure 3.19 C**. However, there was still some measurable ITZ/Ce6@LNPs fluorescence present in the tumor, resulting in a significantly higher accumulation of ITZ/Ce6@LNPs observed in the tumor tissue. it suggests that they are selectively accumulating in the target tissue (superficial skin cancer), which is a desirable outcome for ITZ/Ce6@LNPs gel.

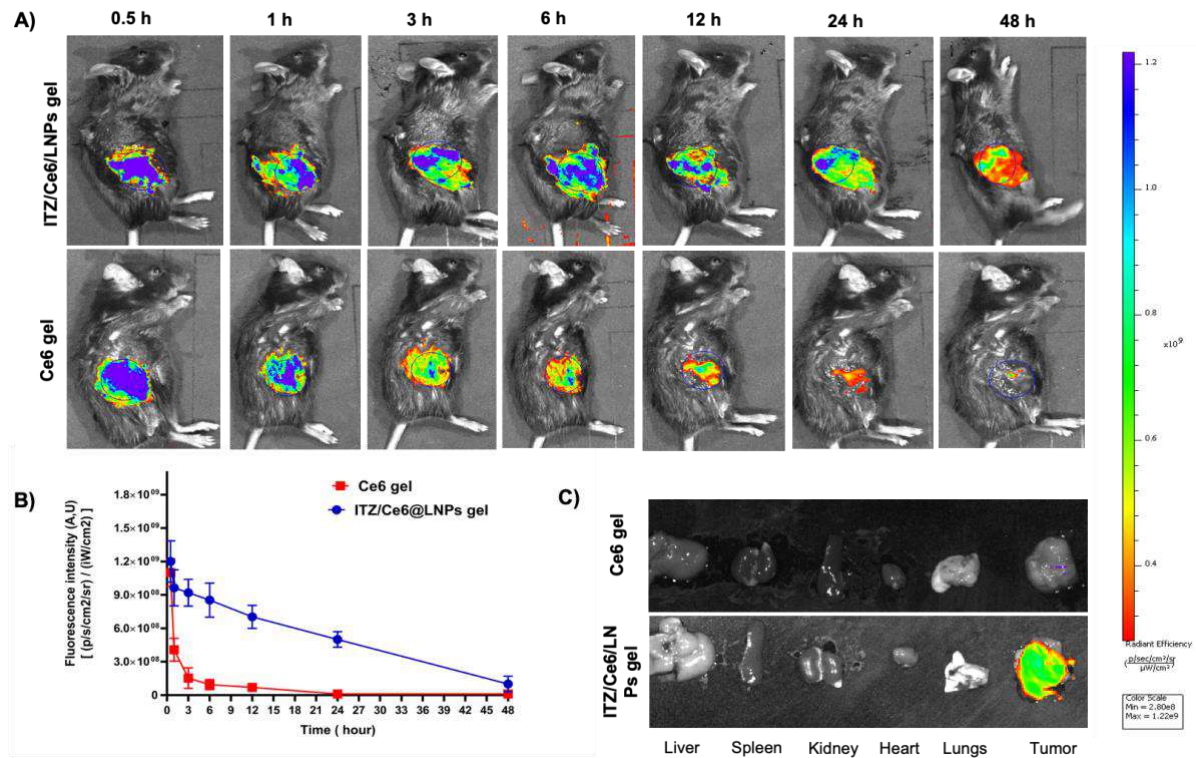


Figure 3.19: In vivo Biodistribution evaluation by IVIS live tumor-bearing mice after topical application of Ce6+ITZ gel, ITZ/Ce6@LNPs gel at various predetermined time points (0.5 h to 48 h) (A); The fluorescence intensity for the region of interest (tumor-bearing mice) was recorded as total photon counts per tumor (B); Ex vivo NIR fluorescence images of major organs and tumor excised at 48 h post-treatment of topical gel (with Ce6+ITZ gel, ITZ/Ce6@LNPs gel) (C).

3.3.6.4. In vivo antitumor activity of ITZ/Ce6/LNPs gel

To assess the in vivo anticancer potential of the ITZ/Ce6/LNPs gel, we conducted experiments following the promising results obtained from the combined chemo-photodynamic therapy in vitro. The tumor volume growth rate was observed to be faster in the PBS-treated control (Blank Gel) group compared to the other treated groups. Notably, the ITZ/Ce6/LNPs gel

exhibited the slowest rate of increase in tumor volume. The average tumor volumes at the end of the eight-day period were measured as $708 \pm 31 \text{ mm}^3$, $502 \pm 10 \text{ mm}^3$, $545 \pm 17 \text{ mm}^3$, $402 \pm 10 \text{ mm}^3$, and $170 \pm 18 \text{ mm}^3$ for the control, free Ce6, ITZ, ITZ+Ce6, and ITZ/Ce6/LNPs gel, respectively (**Figure 3.20A and 3.20 B**). Furthermore, we monitored the body weights of the mice throughout the experiment. **Figure 3.20 C** demonstrates that the body weight of the mice in all experimental groups did not show significant changes, indicating good biocompatibility and biosafety of the ITZ/Ce6/LNPs gel when applied in vivo.

Additionally, the tumor weight in the ITZ/Ce6/LNPs gel-treated group was significantly reduced compared to the control, free Ce6, ITZ, and ITZ+Ce6 groups (**Figure 3.20 D**). These findings further support the potential of the ITZ/Ce6/LNPs gel as an effective therapeutic approach for tumor growth inhibition.

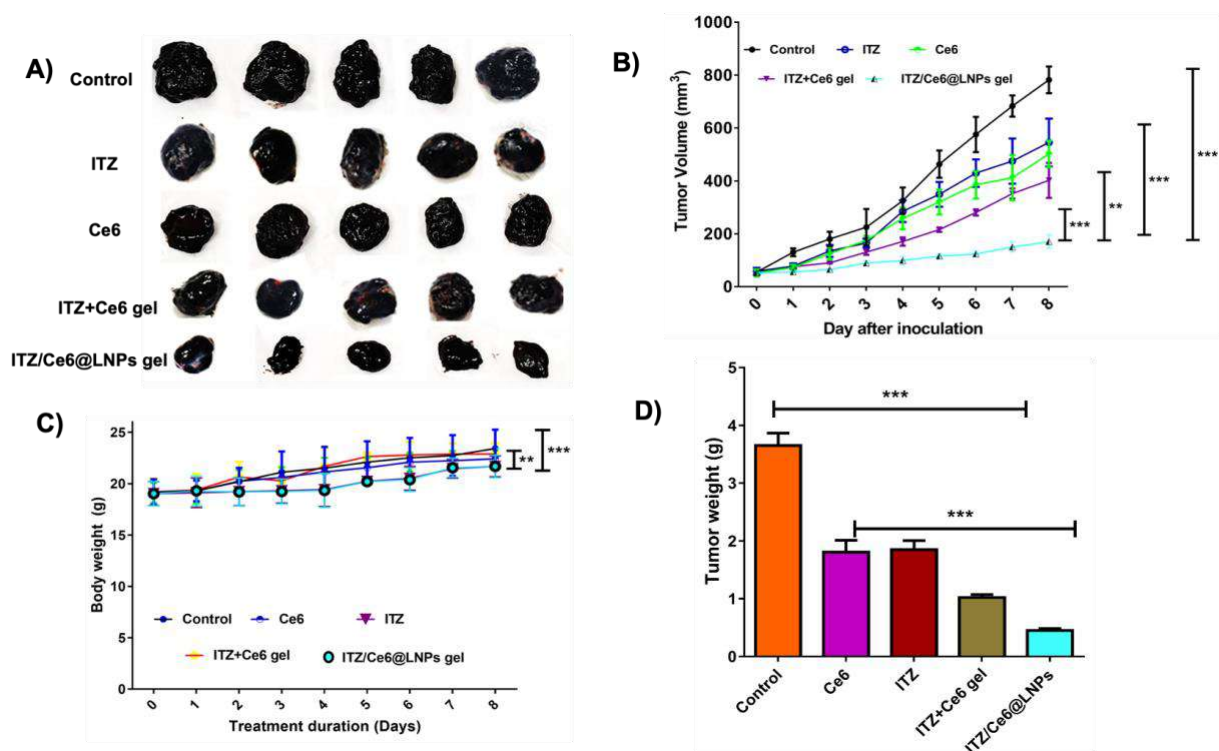


Figure 3.20. Evaluation of in vivo therapeutic efficacy of Ce6, ITZ, ITZ+Ce6 gel, and ITZ/Ce6@LNPs at ITZ equivalent dose of 2.5 mg/kg or a Ce6 dose of 2.5 mg/kg with laser light (666 nm 0.5 W/cm² for 5 min) in B16F10 tumor-bearing mice. images of tumors collected randomly from mice that received treatment as mentioned (A); Graph representing the tumor volume reduction over time. (B); Graphical representation of the body weight over time (C); a Bar graph representing tumor weight of individual groups after study (D) ***p < 0.005.

3.3.6.5. Immunohistochemical Analysis

To further evaluate the therapeutic effect of the treatments, we performed additional analyses on the tumor tissues. The tumor tissues were stained with DCFDA dye to assess the levels of reactive oxygen species (ROS). The terminal deoxynucleotidyl transferase-mediated dUTP nick end labeling (TUNEL) assay was used to detect apoptotic cells, while Ki-67 immunohistochemistry was employed to identify proliferating cells. These analyses provided valuable insights into the cellular response and therapeutic efficacy of the treatments. Our in-vitro efficacy studies have shown that the combination of ITZ+Ce6 and ITZ/Ce6@LNPs can effectively induce cancer cell death through the generation of ROS. To further investigate the therapeutic effect in an in vivo setting, we conducted a study where tumor tissues were treated with ITZ/Ce6@LNPs and the generation of reactive oxygen species (ROS) was measured using DCFH-DA fluorescence and the IVIS-Lumina in-vivo imaging system. The results of this study are presented in **Figure 3.21 A and B**. Additionally, the ROS and TUNEL assays showed increased green fluorescence in tumor samples treated with ITZ/Ce6@LNPs gel compared to other treatment groups, indicating a higher number of apoptotic cells and significant ROS production. In the Ki-67 assay, higher cell proliferation was observed in the control group (displaying the greenest fluorescence), while the ITZ/Ce6@LNPs gel treatment group showed the least proliferation, indicating reduced tumor growth. These results are presented in **Figure 3.22 A and B**. Furthermore, organ damage in the treatment groups was assessed through hematoxylin and eosin (H&E) staining. No histological damage was observed in other organs, such as the kidney, lungs, spleen, and liver, indicating low toxicity of the formulation (**Figure 3.23**).

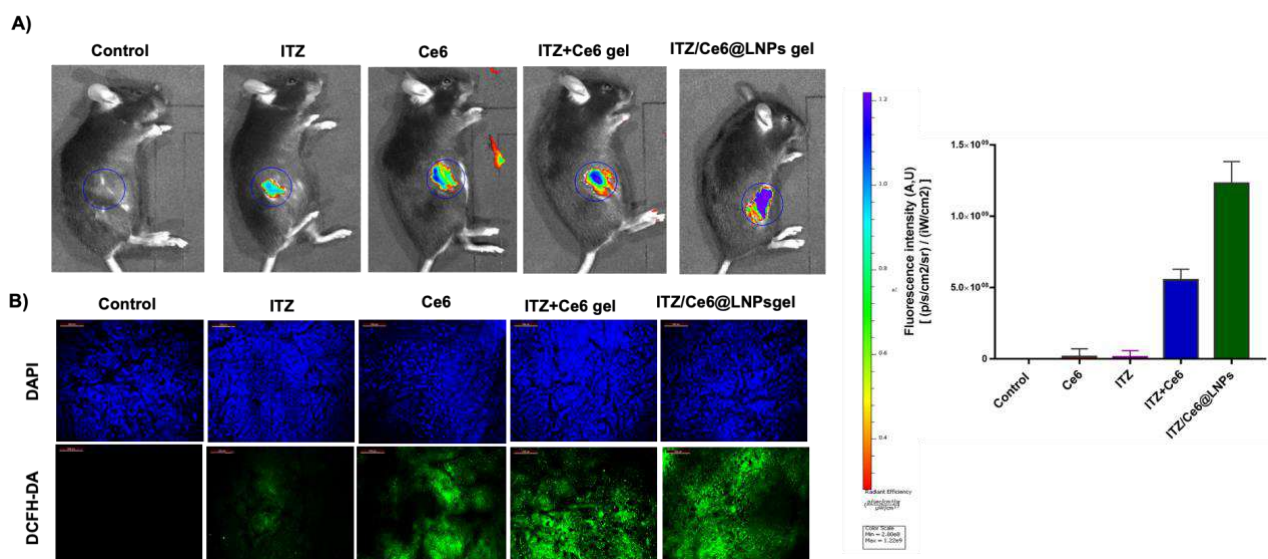


Figure 3.21. In-vivo ROS analysis: DCFH-DA fluorescent images of the whole body of the mice with different treatments (A); Total body fluorescent intensity analysis. DAPI (blue) and DCFH-DA (green) fluorescence images of the sectioned tumor tissues (B).

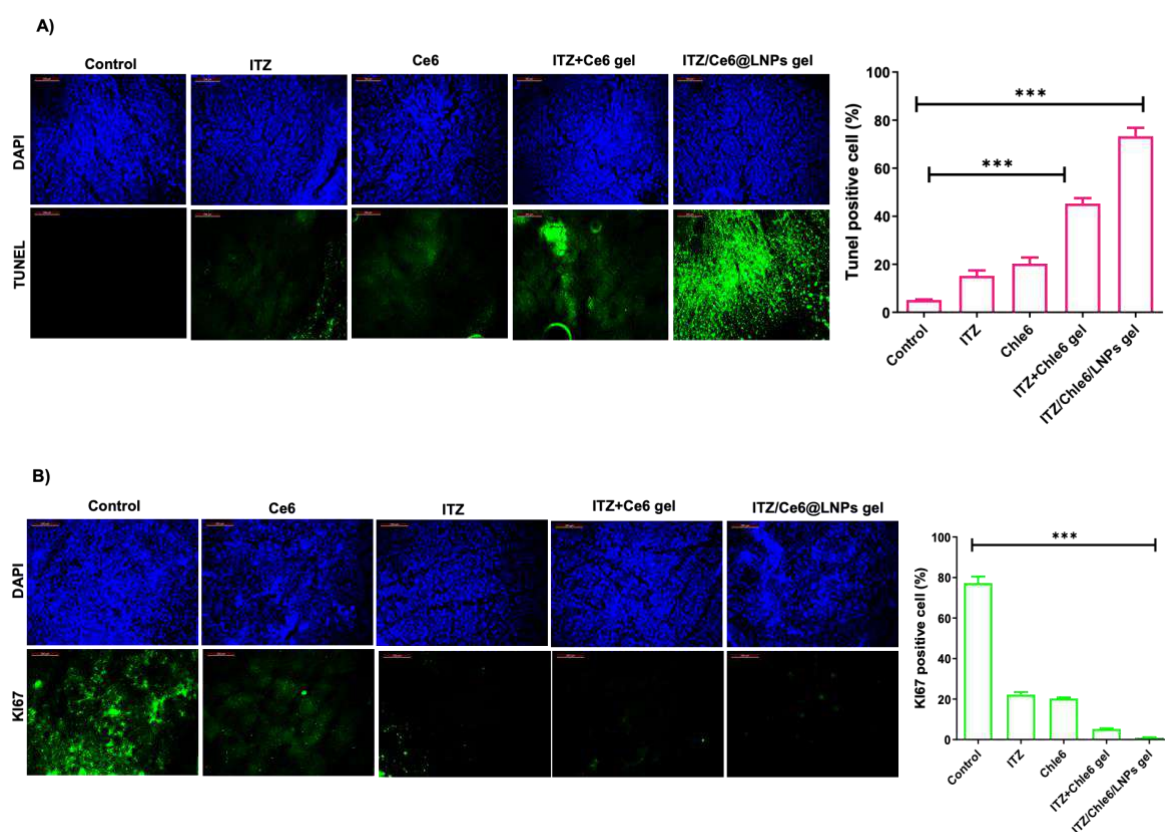


Figure 3.22. Effect of Ce6, ITZ, ITZ+Ce6 gel, and ITZ/Ce6@LNPs treatment on tumor Evaluation of apoptosis in tumor tissues by TUNEL assay (A); Quantification of fluorescence (TUNEL Positive cells %) from TUNEL assay (B); Evaluation of cell proliferation in tumor

tissues by Ki67 immunohistofluorescence assay (C); Quantification of fluorescence (Ki67 Positive cells %) from Ki67 immunohistofluorescence assay. *** $p < 0.005$.

Conclusion: In summary, photo-triggered ROS-generating dual drug-based lipidic nanostructured particles were designed for synergistic effects against basal cell and melanoma cancer. In this work, chlorine e6 as a photosensitizer and ITZ as an anticancer agent (Repurposing agent) encapsulated in lipid nanocarriers and embedded in the SEPINEO gel to enhance the skin and tumor penetration. The optimized formulation showed a uniform nano-size range with high entrapment efficiency for both drugs. This developed dual-drug formulation gel provided high skin penetration and exhibited higher singlet oxygen generation and stability. The skin retention study showed that ITZ/Ce6@LNPs gel has high skin retention compared to the free drugs (ITZ+Ce6), which was confirmed by the IVIS. On a cellular level, the combined formulation showed an excellent synergetic effect compared to free drugs on the B16F10 and A431 cell lines. Moreover, a cellular uptake study with B16F10 and A431 revealed that ITZ/Ce6@LNPs show higher cellular uptake than free drugs. The in vivo antitumor efficacy study demonstrated a significant reduction in tumor weight in the group treated with ITZ/Ce6/LNPs gel compared to the control, free Ce6, ITZ, and ITZ+Ce6 groups. The combination of ITZ and Ce6 delivery by a lipidic system exhibits more therapeutic efficiency than the individual treatment. This lipidic system may provide a unique platform for delivering potent hydrophobic moiety for different ill conditions such as cancer, psoriasis, skin infections, etc. It may also be adequate for clinical testing and commercial application.

Impact of skin cancer research and photodynamic therapy in the advancement of knowledge or benefit to mankind

Skin cancer research and photodynamic therapy (PDT) have significantly contributed to the advancement of knowledge and the benefit to mankind in several ways.

Firstly, skin cancer research has deepened our understanding of the causes, risk factors, and mechanisms behind various types of skin cancer, such as melanoma, basal cell carcinoma, and squamous cell carcinoma. This knowledge has led to the development of better prevention strategies, early detection methods, and more effective treatments. It has also helped identify high-risk populations, such as individuals with fair skin or a family history of skin cancer, allowing for targeted interventions.

Secondly, photodynamic therapy (PDT) has emerged as a valuable treatment option for certain skin cancers, as well as other medical conditions. PDT involves the use of photosensitizing agents and light to selectively target and destroy cancer cells or abnormal tissue. It offers a minimally invasive, precise, and relatively non-toxic approach compared to traditional treatments like surgery or chemotherapy. PDT has revolutionized dermatology and oncology by providing an alternative option for patients, particularly those with superficial skin cancers or precancerous lesions, reducing scarring and improving cosmetic outcomes.

Furthermore, PDT has extended its applications beyond skin cancer treatment. It is now utilized in the management of conditions like actinic keratosis, certain types of acne, and even in the field of ophthalmology for treating macular degeneration. This versatility highlights the broader impact of PDT in medical science.

In summary, skin cancer research and photodynamic therapy have synergistically advanced our understanding of skin cancers, improved patient outcomes, and paved the way for innovative treatments that benefit mankind not only in the realm of dermatology but also in various other medical disciplines. These advancements have not only saved lives but have also enhanced the quality of life for countless individuals by offering less invasive and more effective treatment options.

References :

- [1] P. Koelblinger, R. Lang, New developments in the treatment of basal cell carcinoma: Update on current and emerging treatment options with a focus on vismodegib, *Oncotargets Ther.* 11 (2018) 8327–8340. <https://doi.org/10.2147/OTT.S135650>.
- [2] S. Lucena, N. Salazar, T. Gracia-Cazaña, A. Zamarrón, S. González, Á. Juarranz, Y. Gilaberte, Combined Treatments with Photodynamic Therapy for Non-Melanoma Skin Cancer, *Int J Mol Sci.* 16 (2015) 25912–25933. <https://doi.org/10.3390/ijms161025912>.
- [3] Basal cell carcinoma pathogenesis and therapy involving hedgehog signaling and beyond, (n.d.). <https://www.ncbi.nlm.nih.gov/pmc/articles/PMC5962346/> (accessed January 28, 2021).
- [4] A. Bakshi, S.C. Chaudhary, M. Rana, C.A. Elmets, M. Athar, Basal cell carcinoma pathogenesis and therapy involving hedgehog signaling and beyond, *Mol Carcinog.* 56 (2017) 2543–2557. <https://doi.org/10.1002/mc.22690>.
- [5] N. Mahindroo, C. Punchihewa, N. Fujii, Hedgehog-Gli signaling pathway inhibitors as anticancer agents, *J Med Chem.* 52 (2009) 3829–3845. <https://doi.org/10.1021/jm801420y>.
- [6] M. Wahid, A. Jawed, R.K. Mandal, S.A. Dar, S. Khan, N. Akhter, S. Haque, Vismodegib, itraconazole and sonidegib as hedgehog pathway inhibitors and their relative competencies in the treatment of basal cell carcinomas, *Crit Rev Oncol Hematol.* 98 (2016) 235–241. <https://doi.org/10.1016/j.critrevonc.2015.11.006>.
- [7] R. Pounds, S. Leonard, C. Dawson, S. Kehoe, Repurposing itraconazole for the treatment of cancer (review), *Oncol Lett.* 14 (2017) 2587–2597. <https://doi.org/10.3892/ol.2017.6569>.
- [8] G.K. Sohn, G.P. Kwon, I. Bailey-Healy, A. Mirza, K. Sarin, A. Oro, J.Y. Tang, Topical Itraconazole for the Treatment of Basal Cell Carcinoma in Patients with Basal Cell Nevus Syndrome or High-Frequency Basal Cell Carcinomas: A Phase 2, Open-Label, Placebo-Controlled Trial, *JAMA Dermatol.* 155 (2019) 1078–1080. <https://doi.org/10.1001/jamadermatol.2019.1541>.
- [9] G. Liang, M. Liu, Q. Wang, Y. Shen, H. Mei, D. Li, W. Liu, Itraconazole exerts its anti-melanoma effect by suppressing Hedgehog, Wnt, and PI3K/mTOR signaling pathways, *Oncotarget.* 8 (2017) 28510–28525. <https://doi.org/10.18632/oncotarget.15324>.
- [10] J. Kim, B.T. Aftab, J.Y. Tang, D. Kim, A.H. Lee, M. Rezaee, J. Kim, B. Chen, E.M. King, A. Borodovsky, G.J. Riggins, E.H. Epstein, P.A. Beachy, C.M. Rudin, Itraconazole and Arsenic Trioxide Inhibit Hedgehog Pathway Activation and Tumor Growth Associated with Acquired Resistance to Smoothed Antagonists, *Cancer Cell.* 23 (2013) 23–34. <https://doi.org/10.1016/j.ccr.2012.11.017>.
- [11] J. Kim, J.Y. Tang, R. Gong, J. Kim, J.J. Lee, K. V. Clemons, C.R. Chong, K.S. Chang, M. Fereshteh, D. Gardner, T. Reya, J.O. Liu, E.H. Epstein, D.A. Stevens, P.A. Beachy, Itraconazole, a Commonly Used Antifungal that Inhibits Hedgehog Pathway Activity

- and Cancer Growth, Cancer Cell. 17 (2010) 388–399. <https://doi.org/10.1016/j.ccr.2010.02.027>.
- [12] R. Jain, R. Pradhan, S. Hejmady, G. Singhvi, S.K. Dubey, Fluorescence-based method for sensitive and rapid estimation of chlorin e6 in stealth liposomes for photodynamic therapy against cancer, *Spectrochim Acta A Mol Biomol Spectrosc.* 244 (2021) 118823. <https://doi.org/10.1016/J.SAA.2020.118823>.
- [13] L. Li, B.C. Bae, T.H. Tran, K.H. Yoon, K. Na, K.M. Huh, Self-quenchable biofunctional nanoparticles of heparin–folate-photosensitizer conjugates for photodynamic therapy, *Carbohydr Polym.* 2 (2011) 708–715. <https://doi.org/10.1016/J.CARBPOL.2011.05.011>.
- [14] P. Huang, Z. Li, J. Lin, D. Yang, G. Gao, C. Xu, L. Bao, C. Zhang, K. Wang, H. Song, H. Hu, D. Cui, Photosensitizer-conjugated magnetic nanoparticles for in vivo simultaneous magnetofluorescent imaging and targeting therapy, *Biomaterials.* 32 (2011) 3447–3458. <https://doi.org/10.1016/J.BIOMATERIALS.2011.01.032>.
- [15] C. Yang, H. Chen, J. Zhao, X. Pang, Y. Xi, G. Zhai, Development of a folate-modified curcumin loaded micelle delivery system for cancer targeting, *Colloids Surf B Biointerfaces.* 121 (2014) 206–213. <https://doi.org/10.1016/J.COLSURFB.2014.05.005>.
- [16] S.J. Lee, H. Koo, H. Jeong, M.S. Huh, Y. Choi, S.Y. Jeong, Y. Byun, K. Choi, K. Kim, I.C. Kwon, Comparative study of photosensitizer loaded and conjugated glycol chitosan nanoparticles for cancer therapy, *J Control Release.* 152 (2011) 21–29. <https://doi.org/10.1016/J.JCONREL.2011.03.027>.
- [17] M. Hoebeke, X. Damoiseau, Determination of the singlet oxygen quantum yield of bacteriochlorin a: a comparative study in phosphate buffer and aqueous dispersion of dimiristoyl-L- α -phosphatidylcholine liposomes, *Photochemical & Photobiological Sciences.* 1 (2002) 283–287. <https://doi.org/10.1039/B201081J>.
- [18] V.K. Rapalli, S. Sharma, A. Roy, G. Singhvi, Design and dermatokinetic evaluation of Apremilast loaded nanostructured lipid carriers embedded gel for topical delivery: A potential approach for improved permeation and prolong skin deposition, *Colloids Surf B Biointerfaces.* 206 (2021) 111945. <https://doi.org/10.1016/J.COLSURFB.2021.111945>.
- [19] S.M. Gandhi, A.K. Khan, S. Rathod, R. Jain, S.K. Dubey, D. Ray, V.K. Aswal, A. Joshi, P. Bahadur, S. Tiwari, Water driven transformation of a nonionic microemulsion into liquid crystalline phase: Structural characterizations and drug release behavior, *J Mol Liq.* 326 (2021) 115239. <https://doi.org/10.1016/J.MOLLIQ.2020.115239>.
- [20] S. Kumbham, M. Paul, A. Itoo, B. Ghosh, S. Biswas, Oleanolic acid-conjugated human serum albumin nanoparticles encapsulating doxorubicin as synergistic combination chemotherapy in oropharyngeal carcinoma and melanoma, *Int J Pharm.* 614 (2022). <https://doi.org/10.1016/J.IJPHARM.2022.121479>.
- [21] S. Kumbham, M. Paul, H. Bhatt, B. Ghosh, S. Biswas, Oleanolic acid-conjugated poly (D, L-lactide)-based micelles for effective delivery of doxorubicin and combination

- chemotherapy in oral cancer, *J Mol Liq.* 320 (2020). <https://doi.org/10.1016/J.MOLLIQ.2020.114389>.
- [22] S. Gorantla, E.R. Puppala, V.G.M. Naidu, R.N. Saha, G. Singhvi, Hyaluronic acid-coated proglycosomes for topical delivery of tofacitinib in rheumatoid arthritis condition: Formulation design, in vitro, ex vivo characterization, and in vivo efficacy studies, *Int J Biol Macromol.* (2022). <https://doi.org/10.1016/J.IJBIOMAC.2022.10.117>.
- [23] M. Shah, K. Pathak, Development and Statistical Optimization of Solid Lipid Nanoparticles of Simvastatin by Using 23 Full-Factorial Design, *AAPS PharmSciTech.* 11 (2010) 489. <https://doi.org/10.1208/S12249-010-9414-Z>.
- [24] A. Mancuso, M.C. Cristiano, M. Fresta, D. Torella, D. Paolino, Positively charged lipid as potential tool to influence the fate of ethosomes, *Applied Sciences (Switzerland).* 11 (2021) 7060. <https://doi.org/10.3390/APP11157060/S1>.
- [25] C. Hald Albertsen, J.A. Kulkarni, D. Witzigmann, M. Lind, K. Petersson, J.B. Simonsen, The role of lipid components in lipid nanoparticles for vaccines and gene therapy, *Adv Drug Deliv Rev.* 188 (2022) 114416. <https://doi.org/10.1016/J.ADDR.2022.114416>.
- [26] D.J. McClements, S.M. Jafari, Improving emulsion formation, stability and performance using mixed emulsifiers: A review, *Adv Colloid Interface Sci.* 251 (2018) 55–79. <https://doi.org/10.1016/J.CIS.2017.12.001>.
- [27] S. Uddin, Md.R. Islam, R.Md. Moshikur, R. Wakabayashi, M. Moniruzzaman, M. Goto, Modification with Conventional Surfactants to Improve a Lipid-Based Ionic-Liquid-Associated Transcutaneous Anticancer Vaccine, *Molecules.* 28 (2023) 2969. <https://doi.org/10.3390/MOLECULES28072969>.
- [28] J. Basso, M. Mendes, T. Cova, J. Sousa, A. Pais, A. Fortuna, R. Vitorino, C. Vitorino, A Stepwise Framework for the Systematic Development of Lipid Nanoparticles, *Biomolecules* 2022, Vol. 12, Page 223. 12 (2022) 223. <https://doi.org/10.3390/BIOM12020223>.